



Alexandra Agostinho Gomes Fernandes

Licenciada em Ciências de Engenharia de Micro e
Nanotecnologias

AN ELECTROCHROMIC PAPER-BASED DEVICE AS A DIAGNOSTIC TEST FOR CYSTIC FIBROSIS

Dissertação para obtenção do Grau de Mestre em Engenharia de Micro e
Nanotecnologias

Orientador: Doutora Elvira Maria Correia Fortunato, Professora
Catedrática, Departamento de Ciências dos Materiais,
Faculdade de Ciências e Tecnologias da Universidade
Nova de Lisboa

Co-orientador: Doutor Luís Miguel Nunes Pereira, Professor Auxiliar,
Faculdade de Ciências e Tecnologia da Universidade Nova
de Lisboa

Júri:

Presidente: Prof. Doutor Hugo Águas

Arguente: Prof. Doutor Rui Igreja

Vogal: Prof. Doutora Elvira Fortunato



FACULDADE DE
CIÊNCIAS E TECNOLOGIA
UNIVERSIDADE NOVA DE LISBOA

Setembro 2018

An electrochromic paper-based device as a diagnostic test for Cystic Fibrosis

Copyright © Alexandra Agostinho Gomes Fernandes, 2018.

A Faculdade de Ciências e Tecnologia e a Universidade Nova de Lisboa tem o direito, perpétuo e sem limites geográficos, de arquivar e publicar esta dissertação através de exemplares impressos reproduzidos em papel ou de forma digital, ou por qualquer outro meio conhecido ou que venha a ser inventado, e de a divulgar através de repositórios científicos e de admitir a sua cópia e distribuição com objetivos educacionais ou de investigação, não comerciais, desde que seja dado crédito ao autor e editor.

“A path with flowers never leads to glory.”

Jean de La Fontaine

Acknowledgements

Gostaria de aproveitar esta primeira página para agradecer a todas as pessoas que de alguma forma contribuíram para a conclusão desta etapa da minha vida. Obrigada por tudo!

À Faculdade de Ciências e Tecnologia da Universidade Nova de Lisboa, por ter sido a minha segunda casa nestes últimos anos, e em especial ao Departamento de Ciência dos Materiais. Obrigada pela oportunidade e pela qualidade do ensino.

Ao professor Rodrigo Martins e à professora Elvira Fortunato, não só pela criação do curso de Engenharia de Micro e Nanotecnologias como também pelas excelentes condições em que tive oportunidade de trabalhar, tanto no CENIMAT como no CEMOP. Um especial agradecimento novamente à minha orientadora, professora Elvira Fortunato, e também ao professor Luís Pereira, meu co-orientador. Obrigada por terem disponibilizado este tema, pela inspiração e ajuda ao longo destes meses.

A ti Carolina, por teres sido a minha co-co-orientadora! Obrigada pelo constante apoio e preocupação, pelas ideias e por não me teres deixado desanimar sempre que encontrava obstáculos.

A toda a equipa do CENIMAT pois não podia ter pedido melhor ambiente para trabalhar. Alexandra Gonçalves, Sónia Pereira, Daniela Gomes, Ana Pimentel, Inês Cunha e Paul Grey, obrigada tanto pela vossa competência em todas as análises que precisei como por todas as dúvidas que me conseguiram esclarecer.

A vocês, parceiros de laboratório: Catarina, Nuno, Ricardo, etc. Obrigada pelos desabafos, conselhos, risos e pela companhia. O ambiente no laboratório não seria tão bom sem vocês!

Aos meus compinchas do “Close Space”: Vasco, Farto, Bela, Chico. Obrigada pelo apoio, por todas as parvoíces, pela companhia nos cafés e almoços, ... Por tudo. Tornaram os meus dias maus mais toleráveis. Um agradecimento especial também a vocês “Open Space”!

Ao “pessoal fixe do serrado” e a todos os amigos que fiz ao longo deste curso, obrigada por terem sido a minha segunda família. Ao Cunha, à Cláudia, Zé Raposo, Filipe, Catita e a todos os que me acompanharam no meu ano de caloiira na residência, um obrigada gigante! À minha nano família: Marco, Fernandes, Sara, Pires, Coroa, Inês, Viorel, Oliveira, Cátia, Vasco, Crespo, Jolu, David, Shiv, e a todos os outros que não mencionei. Obrigada por todas as histórias e momentos partilhados nesta longa jornada. Cresci imenso com vocês! E a ti Carolina Costa, um obrigada especial.

Aos meus padrinhos de faculdade, Sofia e Stoi, porque sem vocês não era a mesma coisa! Obrigada madrinha por não me deixares esquecer as minhas origens e obrigada padrinho por me deixares fazer parte da família ainda que um pouco “tarde”. Um agradecimento especial também a vocês afilhados: Ramos, Filipe e Mafalda. Espero aqui pelo vosso sucesso!

À minha família emprestada: Dona Milu, Senhor Aníbal e Senhor Rui. Obrigada por me terem feito sentir em casa e por me terem recebido de braços abertos. Espero um dia conseguir retribuir tudo aquilo que fizeram por mim. Foram, sem dúvida, um grande apoio neste percurso.

À Raquel e à Patrícia, por terem sido as melhores colegas de casa! Depressa se tornaram família e só vos tenho a agradecer por isso.

A ti Safi, por seres como és. Foste a maior surpresa que a margem sul me deu. Obrigada pelos conselhos, pelas palavras amigas e por me teres levado a conhecer sítios incríveis nesta margem!

Às minhas meninas e meninos de Braga, pelos anos de companheirismo: Góis, Ana, Pedro, Ivan e Ricardo. Obrigada por poder contar sempre com vocês e com o vosso apoio, esteja onde estiver!

A ti Alexandre, um obrigada muito especial não só por teres estado sempre presente mas também por todos os puxões de orelhas e abanões que me fizeram acordar. Obrigada pela força, motivação e confiança!

Finalmente, um obrigada do tamanho do mundo à minha família, especialmente aos meus pais, Joaquim e Ana Maria, a quem dedico este trabalho. Devo aos dois a mulher que sou hoje. Obrigada por esta oportunidade, pela confiança que depositaram em mim e pela força que sempre me deram. Espero que, de alguma forma, vos tenha deixado orgulhosos! A ti Patrícia, obrigada por seres uma irmã incansável e um exemplo a seguir. Nada disto seria possível sem o teu apoio. Também à minha tia, Luísa, um agradecimento especial pelas palavras semanais de força e coragem, e aos meus avós, que onde quer que estejam sei que torcem por mim.

Abstract

Cystic Fibrosis (CF) is an inherited disorder affecting more than 70000 people worldwide, especially Caucasian populations with a carrier prevalence of 1/3000. Currently, it has no cure but an early diagnosis remains a critical issue. Sweat chloride test has been the gold standard to diagnose CF since the affected present sweat chloride concentrations ≥ 60 mM. In this work, a planar electrochromic “point-of-care” device, based on tungsten trioxide nanoparticles produced by microwave assisted hydrothermal synthesis, was developed as a first approach for CF diagnostic testing especially in resource-limited environments. For electrodes patterning, a CO₂ laser technology was used in a PET/ITO sheet. The device presents a design that allows the NaCl-based electrolyte deposition, used as artificial sweat, only on time of usage directly on the nanoparticles or in a paper pad. By applying an operating voltage of -3 V, the nanoparticles change their optical properties according to NaCl concentration, presenting a blue colouration with different intensities for different NaCl concentrations. The device was able to differentiate between a positive and negative diagnosis, with a colouration time of only 1 min, using an RGB analysis with a B/R ratio of 1.37 ± 0.03 for 60 mM of NaCl, and a low power consumption.

Keywords: Cystic Fibrosis, sodium sweat detection, hydrothermal synthesis, electrochromic device, tungsten trioxide nanoparticles, colourimetric detection.

Resumo

A Fibrose Quística (FQ) é um distúrbio hereditário que afeta mais de 70000 pessoas mundialmente, especialmente populações caucasianas com uma prevalência de portadores de 1/3000. Atualmente não tem cura, mas o diagnóstico precoce continua a ser uma questão crucial. O teste de cloreto no suor tem sido o padrão para diagnosticar a FQ, uma vez que os afetados apresentam concentrações de cloreto no suor ≥ 60 mM. Neste trabalho, um dispositivo *point-of-care* eletrocromico planar, baseado em nanopartículas de trióxido de tungstênio produzidas por síntese hidrotermal assistida por microondas, foi desenvolvido como uma primeira abordagem para um teste de diagnóstico da FQ especialmente em ambientes com recursos limitados. Para a padronização dos elétrodos foi utilizada uma tecnologia de laser CO₂ numa folha de PET/ITO. O dispositivo apresenta um *design* que permite a deposição do eletrólito à base de NaCl, usado como suor artificial, apenas no momento de utilização, diretamente nas nanopartículas ou num papel. Ao aplicar uma tensão operacional de -3 V, as nanopartículas alteram as suas propriedades óticas consoante a concentração de NaCl, apresentando uma coloração azul com diferentes intensidades para diferentes concentrações de NaCl. O dispositivo foi capaz de diferenciar entre um diagnóstico positivo e negativo, com um tempo de coloração de apenas 1 min, utilizando uma análise RGB com um rácio B/R de 1.37 ± 0.03 para 60 mM de NaCl, e um baixo consumo energético.

Palavras-chave: Fibrose Quística, deteção de sódio no suor, síntese hidrotermal, dispositivo eletrocromico, nanopartículas de trióxido de tungstênio, deteção colorimétrica.

Abbreviations

ABC	ATP-binding cassette
a.u.	Arbitrary unit
ATP	Adenosine Triphosphate
B/R	Blue and Red channels ratio
CE	Counter electrode
CF	Cystic Fibrosis
CFF	Cystic Fibrosis Foundation
CFTR	Cystic Fibrosis Transmembrane Conductance Regulator
CLSI	Clinical and Laboratory Standards Institute
ECFS	European Cystic Fibrosis Society
EDS	Energy Dispersive X-Ray Spectroscopy
EGBE	Ethylene Glycol Butyl Ether
ENaC	Epithelial Sodium Channel
FTIR	Fourier-Transform Infrared Spectroscopy
HS	Hydrothermal Synthesis
<i>h</i>-WO₃	Hexagonal WO ₃
ICDD	International Centre for Diffraction Data
ICM	Intestinal Current Measurement
ISE	Ion Selective Electrode
ITO	Indium Tin Oxide
MAHS	Microwave-Assisted Hydrothermal Synthesis
MSDs	Membrane-Spanning Domains
MVCC	Mutation of Varying Clinical Consequence
<i>m</i>-WO₃	Monoclinic WO ₃
NBDs	Nucleotide-Binding Domains
NBS	Newborn Bloodspot Screening
NPD	Nasal Potential Difference
NPs	Nanoparticles
α-WO₃·0.33H₂O	Hydrated Orthorhombic WO ₃
PC	Polycarbonate
PEO	Polyethylene Oxide
PET	Polyethylene Terephthalate
PG	Propylene Glycol
POC	Point-of-care
PPI	Pulses per inch
PVP	Polyvinylpyrrolidone
Q	Charge
QPIT	Quantitative Pilocarpine Iontophoresis Testing
R	Regulatory domain
RGB	Red Green Blue
SDA	Structure-directing agent
SEM	Scanning Electron Microscopy
TCO	Transparent conductive oxide
t	Time

WE Working electrode
XRD X-Ray Diffraction

Table of contents

<i>Acknowledgements</i>	vii
<i>Abstract</i>	ix
<i>Resumo</i>	xi
<i>Abbreviations</i>	xiii
<i>List of Figures</i>	xvii
<i>List of Tables</i>	xix
Motivation and Objectives	1
Work strategy	1
Chapter I: Introduction	3
1. Cystic Fibrosis	3
1.1. CF diagnostic	3
2. Electrochromism: fundamentals and applications	5
2.1. Tungsten trioxide	6
2.1.1. Hydrothermal synthesis	7
Chapter II: Experimental Methods	9
1. WO ₃ NPs production	9
2. Devices' production	9
3. WO ₃ NPs characterization	10
4. Devices' characterization	10
Chapter III: Results and Discussion	11
1. WO ₃ NPs synthesis and characterization	11
1.1. MAHS optimization process	11
1.1.1. SEM analysis	14
1.1.2. Raman spectroscopy	15
1.2. WO ₃ NPs by HS	16
1.2.1. XRD analysis	17
1.2.2. SEM analysis	17
2. Devices' production	18
2.1. Preliminary tests	18
3. Devices' characterization	20
3.1. Colourimetric analysis	21
3.1.1. Selectivity tests	23
3.2. Electrochemical characterization	24
3.3. Final device	26
Chapter IV: Conclusions and Future Perspectives	29
References	31
Appendices	35

An electrochromic paper-based device as a diagnostic test for Cystic Fibrosis

A. CFTR protein.....	35
B. WO ₃ crystallographic structures: monoclinic, orthorhombic and hexagonal.....	36
C. Materials.....	37
D. NaCl-based electrolytes' preparation.....	38
E. XRD analysis.....	39
F. Cyclic voltammetry.....	40
G. Published posters.....	41

List of Figures

Figure 1: Diagram developed by CFF to standardize the correct way to diagnose CF. [21]	4
Figure 2: Schematic of a typical electrochromic device. Adapted from [45].	5
Figure 3: Crystal structure of WO ₃ : (a) the ideal cubic structure; and (b) the WO ₆ octahedra. [54]	7
Figure 4: a) Layout of the final device and its dimensions with a= 0.1 cm and b= 0.07 cm. b) Schematic representation of the device production: 1. ITO layer etching; 2. WO ₃ NPs deposition; 3. Hydrophilic paper encapsulation. Adapted from [50].	9
Figure 5: Observations from the synthesis of WO ₃ NPs by MAHS. a) Precipitation of tungstic acid after the addition of HCl in WN1 sample. b) WN1, c) WN2, and d) WN3 samples obtained using the “Fixed Power” programme at 100 W.	12
Figure 6: Diffractograms of the three WO ₃ NPs samples produced by MAHS, using the “Fixed Power” programme at 100 W. Peaks marked with \diamond and \blacklozenge are characteristic of H ₂ WO ₄ ·nH ₂ O and <i>m</i> -WO ₃ crystallographic structures, respectively.	12
Figure 7: Powders obtained using the “Dynamic” programme at 160 °C during 40 min for a) WN1, b) WN2, and c) WN3; and at 180 °C during 1 h for d) WN1, e) WN2, and f) WN3. The vessels here presented have a maximum volume of 10 mL.	13
Figure 8: Diffractograms of the three WO ₃ NPs samples produced by MAHS using the: a) “Dynamic” programme at 160 °C for 40 min; and d) “Dynamic” programme at 180 °C for 1 h. Peaks marked with \diamond are characteristic of H ₂ WO ₄ ·nH ₂ O crystallographic structure.	13
Figure 9: SEM images of the three different samples (WN1, WN2, and WN3) produced using the “Fixed Power” programme at 100 W, and using the “Dynamic” programme at 180 °C for 1 h.	15
Figure 10: Raman spectra of WN1, WN2, and WN3 samples. The spectra were collected with a 633 nm laser, at 1% and 3 accumulations.	16
Figure 11: Diffractogram of WO ₃ NPs sample produced by HS at 180 °C for 1 h. The diffractogram represented in black is the crystallographic file deposited in the ICDD data base with the reference #98-003-7822 for hydrated orthorhombic crystallographic structure of WO ₃ . Peaks marked with \diamond are characteristic of H ₂ WO ₄ ·nH ₂ O and peaks with \circ are non-identifiable.	17
Figure 12: SEM images of the sample produced by HS at 180 °C for 1 h, with different magnifications. ...	17
Figure 13: Devices obtained throughout the production process: a) after laser etching of ITO, and b) after deposition and curing of Ag ink.	18
Figure 14: Observations during the preliminary tests of the devices before their encapsulation and after a colouration of 10 min. a) WO ₃ NPs dispersion produced by method 1; b) Deposition of two 2 μ L drops of WO ₃ NPs dispersion produced by method 2; c) Drying process using the hot plate of the WO ₃ NPs dispersion produced by method 2.	18
Figure 15: Colouration tests of the four deposited WO ₃ NPs samples (c=0.04 g/mL) at an operating voltage of -3 V during 30 min.	19
Figure 16: Colouration obtained at an operating voltage of -3 V during 6 min of the samples WN2, WN3 and HS 180 °C (c=0.04 g/mL) using the electrolyte composed by PG and NaCl at 60 mM.	20
Figure 17: Colouration tests of the <i>h</i> -WO ₃ NPs (c=0.06 g/mL and c=0.08 g/mL) at an operating voltage of -3 V during 6 min, using the electrolyte composed by PEO, PVP, PG, and NaCl at 60 mM.	20
Figure 18: Appearance of: a) the devices after the deposition of the WO ₃ NPs and before encapsulation; and b) the bottom and top view of the final devices.	20
Figure 19: SEM (a) and EDS analysis (b, c), and d)) of the interface WE/etched PET/ITO area/ITO area/CE of a device with a WO ₃ NPs concentration of 0.06 g/mL, before encapsulation.	21
Figure 20: Results obtained from the RGB analysis of the devices before encapsulation, for a concentration of WO ₃ NPS of: a) 0.06 g/mL; and b) 0.08 g/mL.	21

Figure 21: a) Results obtained from the RGB analysis of the devices after encapsulation, for a concentration of WO_3 NPs of 0.06 g/mL; and b) Comparison between the B/R values obtained for the devices with a concentration of WO_3 NPs of 0.06 g/mL before (1 min of colouration) and after (6 min of colouration) encapsulation, and respective calibration curves. Both images correspond to a device tested with the electrolyte containing 120 mM of NaCl before (left) and after (right) encapsulation.22

Figure 22: Colouration tests of the final devices, before encapsulation, with a WO_3 NPs concentration of 0.06 g/mL, at an operating voltage of -3 V during 6 min, using two electrolytes: one composed by PEO, PVP, PG, and KCl (10 mM), and other by PEO, PVP, PG, and MgO_4S (2 mM).23

Figure 23: Calibration curve obtained with the B/R values of the colouration tests (1 min) performed on the devices before encapsulation, with a concentration of WO_3 NPs of 0.06 g/mL, and using the electrolyte composed by PEO, PVP, PG, NaCl, KCl, and MgO_4S24

Figure 24: Cyclic voltammetry curves obtained for the devices a) before and b) after encapsulation. The measurement was performed using the electrolyte composed by PEO, PVP, PG, and NaCl at 60 mM, from 3 to -3 V at a scan rate of 100 mV/s, during 10 cycles.24

Figure 25: Charge insertion and extraction during consecutive 120 seconds colouration (-3 V) and bleaching (3 V) during the first cycle for the device before encapsulation.25

Figure 26: Cyclic voltammetry curves obtained for the device before encapsulation between -3 and 3 V at different scan rates: 25, 50, 75, 100, and 125 mV/s. The measurement was performed using the electrolyte composed by PEO, PVP, PG, and NaCl at 60 mM.26

Figure 27: Final apparatus needed for the use of the device in the diagnosis of CF: a) a 3 V battery connected to the device and a cell phone for recording the colouration presented by the device after usage; b) calibration curve obtained with the B/R values of the devices after encapsulation with a WO_3 NPs concentration of 0.06 g/mL and a colouration time of 6 min using the electrolyte composed by PEO, PVP, PG and NaCl. The dashed lines represent the B/R values correspondent to the NaCl concentration of 30 and 60 mM, that indicate a negative and positive diagnosis for CF, respectively.27

Figure 28: CFTR protein structure: a) Linear structure; b) 3D structure in the cell membrane. [3]35

Figure 29: Crystallographic structures of WO_3 : monoclinic, orthorhombic, and hexagonal. Adapted from [78].36

Figure 30: a) Final aspect of the electrolyte produced with PG, PEO, PVP, and a 60 mM concentration of NaCl. b) Formation of the polymer blend between PEO and PVP. The blend occurs through a hydrogen bond between the carbonyl group of PVP and the methylene group of PEO. [79]38

Figure 31: Resume of the synthesis' optimization process using MAHS for sample a) WN1, b) WN2, and c) WN3. The diffractograms represented in black are the crystallographic files deposited in the ICDD data base with the references #98-007-1506, #98-003-7822, and #98-001-3851, for monoclinic, hydrated orthorhombic, and hexagonal crystallographic structures of WO_3 , respectively. Peaks marked with \diamond and \blacklozenge are characteristic of $\text{H}_2\text{WO}_4 \cdot n\text{H}_2\text{O}$ and *m*- WO_3 crystallographic structures, respectively.39

Figure 32: Cyclic voltammetry curves obtained for the devices before encapsulation. Measurements were performed using the electrolyte composed by PEO, PVP, PG, and NaCl at 60 mM, from 3 to -2.5 V during 4 cycles, at a scan rate of a) 25 mV/s, b) 50 mV/s, c) 75 mV/s, d) 100 mV/s, and e) 125 mV/s.40

List of Tables

Table 1: Reagents and quantities used for WO ₃ NPs synthesis via MAHS, based on Marques et al. work. [51]	9
Table 2: Conditions tested during the MAHS optimization process.....	11
Table 3: Dimensions obtained for the WO ₃ NPs produced by MAHS with the programmes “Fixed Power” at 100 W and “Dynamic” at 180 °C for 1 h, using the software ImageJ (n=40).	15
Table 4: Costs analysis of the developed device.....	28
Table 5: List of all used reagents and respective chemical formula, purity, CAS, and company.....	37

Motivation and Objectives

Biosensing for medical applications allied to low-cost production procedures have shown surging interest over the 40 or so years. The dominant model of laboratory testing remains the centralised laboratory. However, due to economic pressures as well as the recognition that care needs to be more patient-centered, healthcare is changing. Hence, point-of-care (POC) testing has increased and this growth is likely to continue, delivering less costly care closer to the patient's home. [1]

Diagnostics are of great importance in the health care system and have a critical impact on decision making clinically. Compared with standard laboratory testing, POC diagnostics are facile, rapid, and inexpensive, and thus have great accessibility to resource-limited environments.

Blood analysis remain the gold standard in the diagnosis of several diseases, although blood sampling is invasive and undesirable for most patients. Recently, eccrine sweat has emerged as an alternative biofluid with several sweat analysis devices, eliminating the sampling discomfort. [2]

Cystic Fibrosis (CF) is one of multiple diseases that can be diagnosed through sweat analysis, measuring chloride (Cl⁻) concentration, and remains one of the most common life-limiting autosomal recessive disorders. [3] An early diagnosis of CF facilitates early implementation of therapy, which can significantly improve the prognosis and life quality of the affected patients. However, in Europe, the cost of a sweat test can vary between 20-300 €. [4]

Numerous research groups have developed different methods for the diagnosis of CF. The trend is to produce a low-cost device that provides reliable results, but only few choose to implement a colourimetric detection by taking advantage of chromogenic materials.

Tungsten trioxide (WO₃) is a very promising material and one of the most studied electrochromic inorganic materials. This interest is regarding its low cost, improved stability, high colouration efficiency, high sensitivity, selectivity, and biocompatibility. As such, it is used in a multiple range of applications in environmental engineering, optoelectronics, microelectronics, selective catalysis, and even biosensing for medical applications. [5]–[7]

With this in mind, the main goal of this work was the development of an electrochromic POC device, based on WO₃ nanoparticles, for a facile diagnosis of CF especially in resource-limited environments. The final device cost was reduced by using alternative methods of production.

Work strategy

The present work was divided in three main stages:

- (i) Synthesis of WO₃ nanoparticles (NPs) by hydrothermal synthesis (HS) and microwave assisted hydrothermal synthesis (MAHS), and respective characterizations. The NPs produced by MAHS went through an optimization process that consisted in the variation of microwave programme, synthesis' temperature, pressure, power, and time;
- (ii) Fabrication of the device and realization of some preliminary tests to choose the best crystallographic structure of the WO₃ NPs for the final application. Several steps related with the deposition of the NPs in the devices were optimized: the method used in the dispersions' production, the concentration of NPs, the quantity of the dispersion for each device, and the drying process;
- (iii) Proof of concept with the diagnosis of CF, performing colourimetric analysis with a NaCl-based electrolyte with different concentrations (0, 30, 45, 60, 75, 90, and 120 mM), acting as artificial sweat, on the devices. Furthermore, it was also studied the influence of common interferents in sweat, to test the selectivity of the device, and an electrochemical characterization was also performed.

Chapter I: Introduction

1. Cystic Fibrosis

CF, also known as mucoviscidosis, is an autosomal recessive monogenetic disorder caused by mutations in the Cystic Fibrosis Transmembrane Conductance Regulator (CFTR) gene. [3], [8] Thus, in order to have CF a person must inherit two copies of the CFTR gene both with mutations (one copy from each parent). People who inherit only one defective gene are called CF carriers: they do not have the disease but can pass their copy on to their children. [9]

This pathology was first identified by Dorothy Andersen, in 1938, and quickly became one of the most common genetic disorders, affecting more than 70000 people worldwide. Its incidence varies according to race and ethnicity being the Caucasian population the most affected, with a carrier prevalence of 1/3000. [3], [10] In Portugal, around 30-40 children are born with CF every year. [8] Currently, there's no cure for it but improvements in diagnostic methods have allowed a more successful management of CF and led to an increased life expectancy of 40-50 years. [3] Furthermore, research on gene therapies is growing and it has been already developed some CF-modifying therapies like CFTR modulators. They have not been approved for use, though. [11]

CF progression depends on the severity of the mutation, and so far, up to 1900 mutations in the CFTR gene have been described and organized into 6 classes that reflect their functional consequences. Class II mutations include the most common one, F508del, presenting a frequency of around 90% worldwide. [3], [11]

The gene involved in this pathology, CFTR, is located in the long arm of chromosome 7 and it encodes for a transmembrane protein also designated CFTR (described in section A of Appendices). This protein acts as a Cl⁻ channel that transports ions across the apical membrane of epithelial cells but also has other functions including bicarbonate secretion and inhibition of sodium (Na⁺) transport. As a member of the Adenosine triphosphate (ATP)-binding cassette (ABC) transporter family, this protein uses energy released by ATP hydrolysis to move substrates (ions in this case) against their electrochemical gradient. Multiple studies reported that CFTR also regulates the activity of the epithelial sodium channel (ENaC). Therefore, CFTR dysfunction restricts the reabsorption of Cl⁻ (and subsequently Na⁺) in the reabsorptive duct of the sweat gland, a process that normally occurs in healthy individuals, as well as the transport of bicarbonate. As a result, in addition to a high NaCl concentration in sweat being an effective evidence of CF, this dysfunction leads to the production of an abnormal viscous secretion in several organs. [11]–[13] This mucus particularly blocks the lungs and causes persistent lung infections due to germs' multiplication, being lung disease responsible for the majority of mortality. [9] However, its phenotype extends to multiple organs. In the pancreas, mucus prevents the release of digestive enzymes that later results in pancreatic insufficiency, gastrointestinal malabsorption, intestinal abnormalities, malnutrition and poor growth. It can also cause liver disease, diabetes, azoospermia in 98% of the affected males, renal complications, salt and water depletion, among others. [3], [10]

1.1. CF diagnostic

A complete diagnostic evaluation for CF includes a sweat test (in support of the newborn bloodspot screening (NBS)), a genetic test, and a clinical evaluation. [10] It is noteworthy that in Portugal, since 2013, CF is included in the so-called “teste do pezinho”, an early diagnostic test for several diseases. [14]

For 60 years, sweat tests have been the gold-standard to diagnose CF and the most employed one is the quantitative pilocarpine iontophoresis testing (QPIT), which consists in the determination of Cl⁻ concentration in sweat. It was originally introduced in 1959 by Gibson and Cooke, and nowadays is implemented by following the Clinical and Laboratory Standards Institute (CLSI) 2009 Guidelines. [12] Perspiration is locally induced on the forearm skin through the administration of pilocarpine nitrate and then, an electric current is applied to stimulate the sweat glands. Sweat is usually collected on a gauze or filter paper (both requiring about 75 mg of sweat), and more recently in a Macroduct® coil (15 µL) for 30 min, and a minimum sweat rate of 1 g/m²/min is required. Then, Cl⁻ levels are generally measured using coulometry (chloridometer). [15]–[17] Concentrations below 30 mmol/L are considered negative for CF and positive above 60 mmol/L. However, there is a range of inaccurate diagnosis for concentrations between 30 and 60 mmol/L and patients within this range are classified as indeterminate cases, requiring further

evaluation. To confirm the veracity of these values, in 2014, Rowe et al. evaluated sweat Cl^- levels as a function of predicted CFTR activity and concluded that healthy adults had a mean sweat Cl^- concentration of 20 mmol/L, CF carriers presented mean levels of 26 mmol/L, CF patients with one severe and one mild CFTR mutation had an average of 80 mmol/L, and patients with two severe mutations had an average in excess of 100 mmol/L. [11], [18]

For indeterminate cases and also to standardize CF diagnosis worldwide, CFF developed a diagram of diagnostic steps presented in Figure 1. [13], [18]–[21]

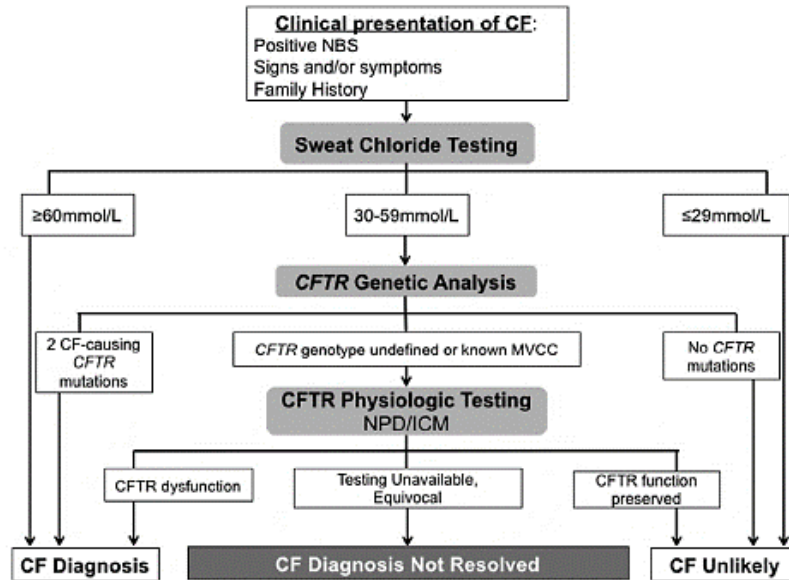


Figure 1: Diagram developed by CFF to standardize the correct way to diagnose CF. [21]

The tests may not be done in this order, but hierarchically to establish the diagnosis of CF, sweat test should be done first, then CFTR genetic analysis, and finally CFTR physiologic tests. The final result of CFTR genetic analysis may be a known mutation of varying clinical consequence (MVCC). This means that combined with a CF-causing mutation or another MVCC, the mutation may result in CF. For that reason, a nasal potential difference (NPD) test or an intestinal current measurement (ICM) test is needed to reach or not the CF diagnosis. [21]

Besides the intermediate range uncertainty and the amount of sweat required, the Gibson and Cooke QPIT also requires experienced staff and procedures like sweat collection are liable of failure, leading to a high frequency of technical errors. So, the development of new, low-cost, POC and portable devices for CF diagnosis is of great importance. [12] Gonzalo-Ruiz et al. developed a disposable screen-printed sensor device to induce sweat and measure the Cl^- concentration by potentiometry for CF detection. [22] Schazmann et al. described a Na^+ sensor belt based on a Na^+ Ion Selective Electrode (ISE). [23] Wang et al. developed a device for Cl^- concentration detection using the fluorescence intensity of a Cl^- ion fluorescent indicator. [24] Bandodkar et al. showed an epidermal temporary-transfer tattoo-based potentiometric sensor coupled to a wireless transceiver for real-time monitoring of Na^+ , but no specific disease is addressed. [25] In 2014, Rock et al. reported a method for quantitative sweat Cl^- determination, the CF Quantum® sweat test, which uses an ion exchange reaction between sweat Cl^- anions and silver chromate. It is not a POC device though. [26] Mu et al. developed a colourimetric paper-based device for CF screening, directly on skin, combining both anion exchange and pH test papers. However it is not selective. [27] In 2016, Gao et al. reported a wearable Bluetooth-enabled band containing a panel of sensors for sweat electrolytes including Na^+ , which is measured through the use of ISEs. [28] De Matteis et al. showed a POC electrochromic device capable to diagnose CF, with high selectivity for Na^+ , using the well-known WO_3 . [12] Emaminejad et al. developed a fully integrated wearable platform to stimulate sweat and measure sweat electrolytes like Na^+ and Cl^- , reporting its use for CF diagnosis. [29] Recently, microfluidic devices for sweat electrolyte quantification by colourimetric detection, potentiometry or ISEs have been vigorously developed. Anastasova et al., Matzeu et al., Choi et al., and especially John A. Rogers' research group are some examples. [30]–[35]

2. Electrochromism: fundamentals and applications

As mentioned before, colourimetric detection has been widely explored and represents an attractive way for a rapid detection of multiple analytes. Chromogenic materials are often explored concerning this topic, as they are capable of undergoing controlled reversible changes in their optical response (transmission, absorption, and reflection), generated by an external stimulus which promotes a modification in the material's chemical or physical state. When the external stimulus is an electrical current or potential, the phenomenon is called electrochromism. [36] This property makes them appealing for several applications like electrically switchable rear-view car mirrors for anti-dazzle, reusable price labels, glazing units for temperature and light control, smart windows, and visual displays, to name just a few. [37], [38]

According to Granqvist, a high impact scientist in this specific area, electrochromism is the reversible and persistent change of the optical properties of a material, when an electrical potential is applied to it. [39] The optical absorption of the material is modified through the insertion of both electrons and charge-balancing ions. As such, the principle is based on a redox reaction, and once it is a reversible process, the material has the ability to switch between two distinct oxidation states: the coloured and the bleached state. The colour change is commonly between a transparent and a coloured state, or between two coloured states. [40], [41]

Electrochromic materials embrace both organic and inorganic materials. [42] However, inorganic electrochromic materials have been widely reported in the literature owing to their photochemical stability whereas the organic alternatives may be susceptible to photochemical degradation. [43] Among this group, transition metal oxides stand out, especially WO_3 which is described in section 2.1., as they exhibit both cathodic and anodic colouration phenomenon: colouration under ion insertion (oxidized coloured state) and under ion extraction (reduced coloured state), respectively. [42] Oxides based on vanadium present intermediate electrochromic properties as they are capable of both colouration types. On the contrary, oxides based on tungsten and iridium only undergo cathodic and anodic colouration, respectively. In fact, most electrochromic devices based on oxides employ two electrochromic films, taking advantage of combining cathodic and anodic oxides (WO_3 and $\text{Ni}(\text{OH})_2$ for example). This way, when applying a voltage to transport ions and electrons in one direction, both oxides colour, and when transporting ions and electrons in the other direction, both oxides bleach. Consequently, a more efficient device is obtained. [38]

There are multiple configurations for electrochromic devices, depending on property requirements. A typical electrochromic device schematic is depicted in Figure 2 with four layers between two transparent substrates that are usually from transparent glass or a flexible polyester (polyethylene terephthalate (PET), for example). The substrates are then coated with a transparent conductive oxide (TCO) like indium tin oxide (ITO), being one of them coated with an electrochromic material and the other with an ion storage film, which is not represented in the schematic but was already mentioned as part of most devices. The electrolyte, a pure ionic conductor, separates them. [42], [44]

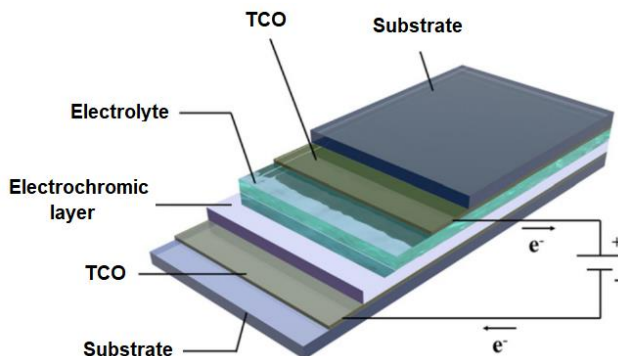


Figure 2: Schematic of a typical electrochromic device. Adapted from [45].

When a voltage is applied between the TCOs, a distributed electrical field is set up on the device and the ions from the electrolyte move uniformly into and out of the electrochromic material. The charge-balancing counterflow of electrons then leads to an electron density's variation in the electrochromic material, leading to a modulation of its optical properties. After the decay of the resulting pulse of current,

if the ion conductor has negligible electronic conductivity, the device will exhibit an open circuit memory (the so-called “memory effect”), and the optical properties remain stable for long periods of time. [41], [44]

The appropriate selection of the electrolyte is one of the key parameters for electrochemical processes, and they may be solid, liquid or elastomeric. Concerning the liquid electrolytes, fluids of high viscosity are usually preferred, for convenience and safety. [40]

Polyethylene oxide (PEO) based electrolytes are among the most studied because of their beneficial structure in supporting fast ion transport. High conductivity seems to be related with the facile dissolution of the cation by the coordination group of the polymer that, in this case, is an ether oxygen. PEO is a semi-crystalline linear polymer, presenting both amorphous and crystalline phases at room temperature. Its chemical structure has series of –O– polar groups which can easily associate with metal cations (Figure 30 b) from section D of Appendices). However, PEO itself presents an extremely low reactivity. [46], [47]

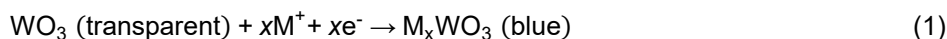
A high crystalline phase concentration limits the conductivity of PEO based electrolytes. One of the most successful approaches to suppress it is the preparation of polymer blends between PEO and an acrylic polymer. Polyvinylpyrrolidone (PVP) is often chosen as it presents an amorphous nature allowing faster ionic mobility (Figure 30 b) from section D of Appendices). Besides, the rigid pyrrolidone group of PVP is known to form various complexes with several inorganic salts. Sodium complexed electrolyte films have been found to exhibit multiple advantages. In fact, the mobility of bigger ions like Na⁺ is higher than that of smaller ions (lithium – Li⁺ – and magnesium – Mg²⁺) in the polymer electrolytes once smaller cations are captured by the polymeric network. [46], [47]

As solvents, common organic ones are normally undesirable due to their inherent toxicity and high flammability. However, propylene glycol (PG) is an example of an organic solvent with low flammability and one of the least toxic of the glycols. [48] Furthermore, it is one of the best solvents for NaCl since the salt presents a solubility of 71 g/kg (at 25 °C) for this solvent. [49]

Many electrochromic devices comprise a sandwich structure of thin layers, including one for the electrolyte. When using liquid electrolytes, there’s a higher probability to deal with risks of leakage, long-term sealing problems and, therefore, a short shelf life of the device. However, their ionic conductivities are higher. [39], [42], [44], [45] As such, to overcome the mentioned drawbacks, an electrochromic device with a planar structure and two electrodes defined as working and counter electrode (WE and CE, respectively) can be a solution, being the WE named this way once the redox reactions occur on the NPs deposited on top of it. [50] The device is produced without any electrolyte, and its deposition, by drop-casting on both electrodes, is only performed on time of usage. Therefore, instead of using an electrolyte layer typical of a stacked multilayer structure, it is used a hydrophilic paper encapsulated inside the device, covering both electrodes. The layout of the device is shown in Figure 4 from the next Chapter, and as can be seen, its planar structure, besides the already mentioned advantages, represents a totally innovative way to produce electrochromic devices, since most part of them comprise the conventional sandwich structure of layers.

2.1. Tungsten trioxide

As already mentioned, WO₃ remains one of the most studied and used electrochromic inorganic materials due to some of its properties like improved stability, high colouration efficiency, high sensitivity, selectivity, and biocompatibility. In addition to its application as an electrochromic material, WO₃ can also be used in pH and gas sensors, photocatalysis, solar energy devices, biosensors, among others. [5]–[7], [51] The electrochromism in this material is based on the following redox reaction [41]:



where M⁺ is a cation of the alkali metal group (H⁺, Li⁺, Na⁺ or K⁺), e⁻ represents an electron and x, the insertion coefficient, indicates the fraction of electro-reduced tungsten sites. As such, when WO₃ integrates electrons and ions, to maintain its electro-neutrality, it can be reversibly transformed into a tungsten bronze (M_xWO₃), with total different properties and which presents a blue colouration. [39], [41], [43]

The crystal structure of WO₃ allows the intercalation of ions, once it presents a considerable interstitial space for the process to occur. WO₃ is formed by a sequence of perovskite-like (WO₆) octahedral building blocks with connecting corners in three dimensions, which can be visualized as an infinite framework of corner-sharing WO₆ octahedra, each with a central tungsten ion (W⁶⁺) surrounded by six equidistant oxygen ions. An ideal WO₃ crystal structure can be considered as a rhenium trioxide (ReO₃)

type cubic structure, as depicted in Figure 3. [42], [52] However, the WO_6 units undergo tilting, rotation, or displacement of the central W atoms, promoting several crystalline modifications to WO_3 . As such, symmetries like hexagonal, cubic, tetragonal, orthorhombic, monoclinic or triclinic, are found, being the last four reversibly transformed into each other by changing the temperature. [53], [54] Among these symmetries, the hexagonal one outstands due to its hexagonal tunnels, that are particularly relevant to the chromogenic behaviour, once the spaces between the WO_6 octahedra are large enough to accommodate ions. [42], [55] In section B of Appendices, a brief description of the monoclinic, orthorhombic and hexagonal structures is presented.

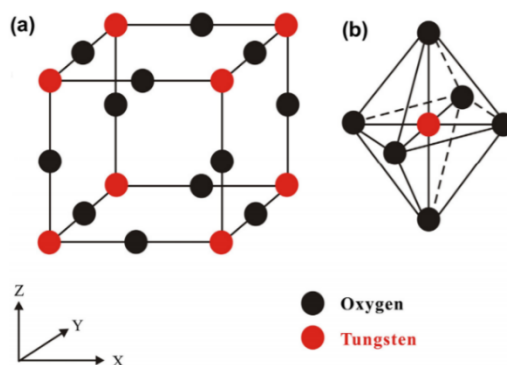


Figure 3: Crystal structure of WO_3 : (a) the ideal cubic structure; and (b) the WO_6 octahedra. [54]

So far, multiple methods have been reported to synthesize nanostructured tungsten oxides with various morphologies: sputtering, temperature annealing, hot wire chemical vapor deposition, pulsed laser irradiation, sol-gel, electrodeposition, precipitation, anodization, and also hydrothermal methods. [5], [56] Among these methods, hydrothermal method is a facile, dominant tool for the synthesis of anisotropic nanoscale materials. [57]

2.1.1. Hydrothermal synthesis

HS is a low-cost method extremely used in the crystallization of substances from high-temperature aqueous solutions (usually below $300\text{ }^\circ\text{C}$) at high vapor pressures, allowing an improved solute dissolution. [58] The crystal growth is performed in a steel pressure vessel (autoclave), in which a reagent is supplied along with water as solvent (precursor solution). The autoclave is then placed in an oven and a gradient of temperature is maintained at its opposite ends. This way, the hotter end dissolves the reagent and the cooler end causes seeds to take additional growth. [59]

This method presents significant advantages regarding the better control over the crystal growth, shape, and size, low synthesis temperature, cost-effectiveness, low number of impurities, improved product yield, and good homogeneity of the nanoparticles synthesized. [5], [51], [57] However, with the reduction of synthesis' temperature, the reaction's kinetic becomes slower. To overcome this issue, hydrothermal hybrid techniques have been developed, being MAHS one of the most popular. Heating in the conventional method is considered inefficient since it depends on the convection currents, and on the thermal conductivity of the materials that must be penetrated, resulting in a discrepant temperature between the autoclave, that has a higher temperature, and the reaction mixture. On the contrary, a material processed in a microwave interacts with the electromagnetic radiation and not with the radiant energy. As the heat is generated by the material itself, being a result of the interaction between the electromagnetic wave and the electric dipole of the mixture's molecules, the temperature of the whole volume is simultaneously raised in a faster and uniform way. [59]–[61] As such, MAHS is a greener approach than HS, once it reduces energy costs.

Concerning the synthesis of WO_3 NPs by HS methods, the use of structure-directing agents (SDAs) to direct and control the crystal growth during synthesis is very common. Multiple SDAs were reported in literature: Na_2SO_4 , $(\text{NH}_4)_2\text{SO}_4$, Li_2SO_4 , and NaCl are some examples. It is believed that capping agents containing sulphate ions dictate an anisotropic one-dimensional growth by selectively binding to specific facets of the initial crystal nuclei of WO_3 . Their adsorption decreases the surface energy of the WO_3 seed crystals in all directions, inhibiting growth rates, except one, which allows the obtention of one-dimensional wire/rod-like structures. [57], [62]

Chapter II: Experimental Methods

It is noteworthy that the information of all used materials is presented in section C of Appendices.

1. WO₃ NPs production

WO₃ NPs were produced via HS and MAHS. For HS, and based on Santos et al. work [6], 0.4 g of Na₂WO₄·2H₂O were dissolved in 8 mL of deionized H₂O and then acidified with 0.83 mL of HCl 3 M. Reagents were mixed for 1 h at 500 rpm while sealed. The mixture was then transferred to a Teflon cup, set inside a stainless-steel autoclave and placed in a L3/11/B170 Nabertherm oven for 1 h at 180 °C, with a heating ramp of 30 min. For MAHS, and based on Marques et al. work [51], WO₃ NPs with three different crystallographic structures were produced, as illustrated in Table 1.

Table 1: Reagents and quantities used for WO₃ NPs synthesis via MAHS, based on Marques et al. work. [51]

Na ₂ WO ₄ ·2H ₂ O (g)	NaCl (g)	H ₂ O (mL)	HCl 3 M (mL)	pH	Crystallographic structure	Nomenclature
0.8	0.36	2	13.33	0.0	Monoclinic	WN1
		16	1.67	1.8	Orthorhombic	WN2
	Na₂SO₄ (g)					
	0.72	16	1.67	1.8	Hexagonal	WN3

For each sample, after adding H₂O to the solid reagents, there was a stirring step of 6 min, and after HCl addition a stirring step of 20 min, both at 500 rpm, and always sealing the recipients. The mixtures were then transferred into a 35 mL microwave vessel, sealed, and heated in a microwave reactor Discover SP from CEM Corporation. All synthesis went through an optimization process varying the microwave programme, temperature, pressure, power, and synthesis' time. After synthesis, the nanopowders obtained were collected by centrifugation at 4000 rpm during 10 min, using a F140 Focus Instruments centrifuge, followed by a washing process with deionized water during a centrifugation of 5 min, and then 2 min. The collecting and washing process was also applied to the HS sample.

Two methods were studied to produce the WO₃ NPs dispersions from HS and MAHS. The first method consisted in drying the final powders, after the washing process, using a "Vacuo-Temp" desiccator (J. P. Selecta) for 10 h at 70 °C, under vacuum. Then, the solids obtained were grounded, using a mortar and pestle to obtain fine powders, and dispersed in a 1:1 mixture of ethylene glycol butyl ether (EGBE) and deionized water. The second method consisted in dispersing the powders, right after the washing process, using the same mixture described for the first method. All dispersions were stored in glass flasks, sealed, and protected from light with aluminium foil. The ideal concentration was also studied and optimized.

2. Devices' production

In Figure 4, it is presented an illustration of a single device layout as well as its dimensions and its main production steps.

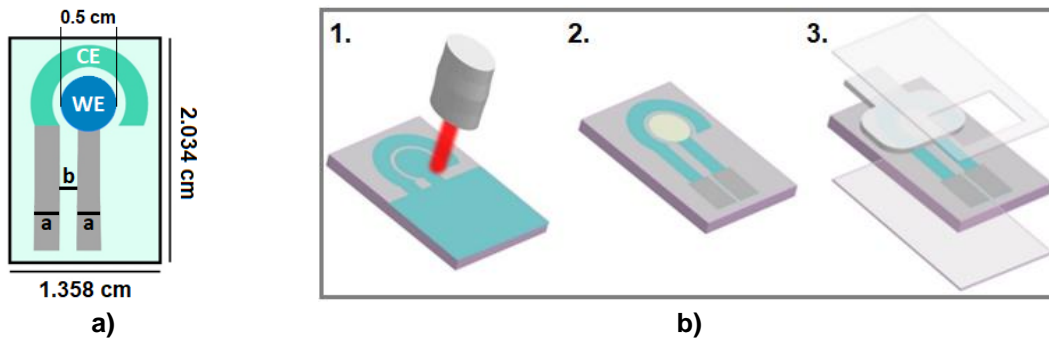


Figure 4: a) Layout of the final device and its dimensions with a= 0.1 cm and b= 0.07 cm. b) Schematic representation of the device production: 1. ITO layer etching; 2. WO₃ NPs deposition; 3. Hydrophilic paper encapsulation. Adapted from [50].

The first production step (Figure 4 b) 1.) was the definition of the electrodes and the electrical tracks of the device. This was achieved by making a negative pattern of them in a PET/ITO sheet by laser etching the ITO layer. The equipment used was a computer-controlled CO₂ Infrared laser-cutting machine VLS 3.50 (Universal LASER systems) with a 10.6 μm wavelength, at 10 W, 1.27 m/s and 1000 PPI (pulses per inch). Then, the patterned sheet went through a 3-step cleaning process: first, with detergent; second, with an ultrasonic bath, using a Sonorex Super RK 514/H (Bandelin), for 10 min with deionized water; and third, also with an ultrasonic bath for 10 min with ethanol. The sheet was finally dried with nitrogen jet.

The second production step (Figure 4 b) 2.) involved the electrical contacts painting with Silver (Ag) conductive ink and the deposition of WO₃ NPs. To simplify this step, the layout of the contacts was cutted into a self-adhesive film, also using the laser-cutting machine at 40 W, 1.016 m/s and 1000 PPI. The film was stucked to the patterned PET/ITO sheet, and the ink was deposited with a brush. The sheet with the devices was then processed on a hot plate (120 °C, 10 min), with no contact with it, for ink curing. After cooling down, the self-adhesive film was removed, and the deposition of WO₃ NPs dispersion was carried out by drop-casting of 2 μL (while stirring) onto the WE, followed by a drying process at room temperature overnight, protected from the light.

The final step (Figure 4 b) 3.) comprised the encapsulation of a hydrophilic paper pad within the device. Using the laser-cutting machine at 40 W, 1.016 m/s and 1000 PPI, Whatman paper grade n.^o4 was cutted into the pattern represented in Figure 4 b) 3.. Lastly, all the devices were encapsulated on plastic laminating pouches using a Mars A4 Laminator (Fellowes), with the hydrophilic papers inside, covering the area of the WE and CE. This only happened after laser patterning the pouches at 3 W, 0.0762 m/s and 1000 PPI, with delimiting lines for a single device, and cutting a square to allow access to the electrical tracks. For the consequent electrolyte impregnation, a small pad was left outside of each device. The final devices were individualized to a dimension of around 1.4 x 2.0 cm.

It is noteworthy that the vector image software Adobe illustrator (Adobe systems software) was used to draw all the layouts employed during this experimental work.

3. WO₃ NPs characterization

The structural characterization of the different WO₃ NPs was performed by X-ray diffraction (XRD) using a PANalyticalX'Pert Pro X-ray diffractometer in Bragg–Brentano geometry, with a monochromatic Cu-Kα radiation source (wavelength 1.5406 Å). All measurements were carried out from 10 to 70° (2θ).

As a supplement for structural analysis, it was used a Renishaw inVia Qontor confocal Raman Microscope using a 633 nm laser (1% power) and a Leica N PLAN L50x/0.50 BD Microscope objective. The time of exposure was 10 s, and spectra was obtained after 3 accumulations.

Finally, the morphology of the WO₃ NPs was analysed by scanning electron microscopy (SEM) using a Carl Zeiss AURIGA Crossbeam (SEM-FIB) workstation instrument.

4. Devices' characterization

To examine the effectiveness of the ITO etching, it was performed an Energy Dispersive X-Ray Spectroscopy (EDS) on a device, with an Oxford INCA x-act coupled to the SEM workstation. Then, to optimize some parameters of production, preliminary tests were carried out before the encapsulation step using a LiClO₄:PC 1 M electrolyte. The electrolyte was drop-casted right on top of the WE and CE, and a DC Power Supply PS-303D-II from ZHAOXIN Electronics Co., Ltd was used at -3 V for 30 min, to assess colour modulation.

For the final characterizations, an electrolyte based on PEO, PVP, PG, and different concentrations of NaCl (0, 30, 45, 60, 75, 90, and 120 mM), to simulate the human sweat, was produced (section D of Appendices) and drop-casted as mentioned above on the devices (before and after encapsulation). Then, it was performed a colourimetric analysis at -3 V for different times, using the aforementioned power supply. The results were recorded with an Apple Iphone X, and colour development analysis was performed with ImageJ software (National Institutes of Health) through a Red Green Blue (RGB) control. It was also studied the influence of common interferents in sweat, using KCl and MgO₄S in the production of other electrolytes (section D of Appendices). For electrochemical characterization, it was used a Gamry 600 Potentiostat from Gamry Instruments, and chronocoulometry and cyclic voltammetry measurements were performed to fully characterize the devices.

Chapter III: Results and Discussion

In this chapter, the results obtained throughout this work are presented and discussed.

Firstly, it is presented the WO₃ NPs synthesis optimization process by MAHS as well as the structural, morphological and chemical characterization of the NPs obtained. The ones obtained by HS are also presented and characterized. Then, the devices production and the results of some preliminary tests realized to optimize the devices are presented and discussed. The chapter ends with the devices' final characterizations: colourimetric study, electrochemical characterization, and some selectivity tests.

1. WO₃ NPs synthesis and characterization

The first step of this work was the optimization of WO₃ NPs production by MAHS, in order to obtain three crystallographic structures: monoclinic, *m*-WO₃ (WN1); hydrated orthorhombic, *o*-WO₃·0.33H₂O (WN2); and hexagonal, *h*-WO₃ (WN3). To achieve these structures, certain parameters were studied: the microwave programme, temperature, pressure, power, and synthesis' time.

The first programme tested was "Fixed Power". Basically, the synthesis occur at a constant power of 100 W for 1 h (maximum) and with a maximum safe temperature of 200 °C, conditions already studied by Marques et al.. [51] A different programme was also tested, "Dynamic", which consisted in a constant temperature of 160 °C, and a dynamic power (200 W maximum) in order to maintain the temperature. The maximum pressure was 300 psi and the programmed synthesis' duration was 40 min. Finally, the last modifications to the programme were the increase of temperature to 180 °C and duration to 1 h, and the decrease of maximum pressure to 280 psi. A resume of all conditions tested in the MAHS optimization process is presented in Table 2.

Table 2: Conditions tested during the MAHS optimization process.

	Microwave programmes		
	Fixed Power	Dynamic	Dynamic
Power (W)	100 (constant)	200 (max.)	
Temperature (°C)	200 (safe)	160 (constant)	180 (constant)
Time (min)	60	40	60
Pressure (psi)	300 (max.)		280 (max.)

In addition to MAHS, HS was also used to produce WO₃ NPs with *o*-WO₃·0.33H₂O crystallographic structure. Although it did not undergo through an optimization process, this synthesis was later tested on the devices along with the ones produced by MAHS with the best conditions.

1.1. MAHS optimization process

During the preparation of the solutions to undergo MAHS, it was possible to notice the precipitation of a white solid right after the addition of HCl (Figure 5 a)). This solid corresponds to tungstic acid, an intermediate product, and its formation was more perceptible in WN1 once this sample presented the lowest pH. For samples WN2 and WN3, the addition of HCl only formed kind of a white mist in the respective mixture.

The formation of this acid is the first of three major steps of WO₃ NPs production. The tungstic acid (H₂WO₄·nH₂O) is produced when the precursor solution is acidified, reason why pH plays such an important role in the formation of WO₃ (Eq. 2). Then, as this product is decomposed, the formation of WO₃ aggregates takes place, as described in Eq. 3, leading to the WO₃ NPs grow. All synthesis were produced with a pH bellow 2, because for higher values the formation of the acid does not occur. [62]–[64]

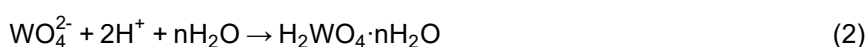


Figure 5 b), c), and d) represent the final result of the synthesis using the "Fixed Power" programme at 100 W during 1 h for each sample.

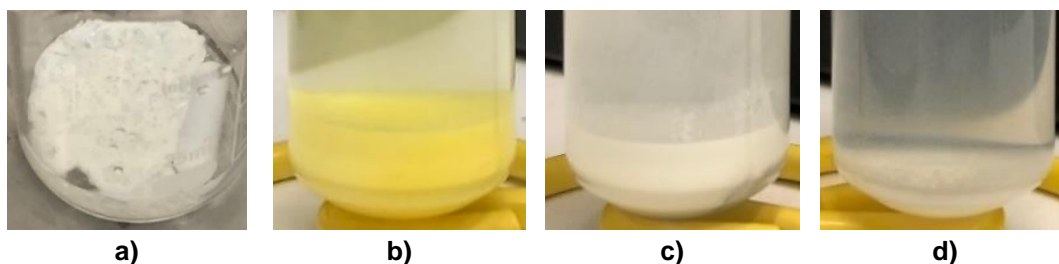


Figure 5: Observations from the synthesis of WO_3 NPs by MAHS. a) Precipitation of tungstic acid after the addition of HCl in WN1 sample. b) WN1, c) WN2, and d) WN3 samples obtained using the “Fixed Power” programme at 100 W.

All three samples did not achieve a synthesis' time of 1 h. The maximum time was obtained for WN3 sample and the minimum for WN1.

The difference between the yield of the three samples is remarkable. WN1 and WN2 presented close yields and higher than the one of WN3, which was very low. This fact can be associated with the synthesis' conditions, once the maximum synthesis' time of WN3 sample was 15 min. Probably, this time was not enough to allow the total reaction between reagents. Besides this difference, there was also a difference between the colours obtained. WN1 sample presented a yellow colouration, characteristic of the monoclinic crystallographic structure, while WN2 and WN3 presented a white one.

To analyse the crystallographic structures obtained for each sample, XRD analysis were performed and are presented in Figure 6.

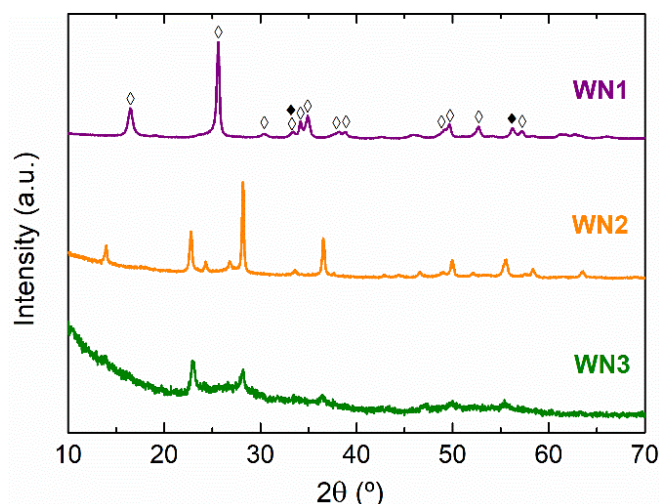


Figure 6: Diffractograms of the three WO_3 NPs samples produced by MAHS, using the “Fixed Power” programme at 100 W. Peaks marked with \diamond and \diamond are characteristic of $\text{H}_2\text{WO}_4 \cdot n\text{H}_2\text{O}$ and $m\text{-WO}_3$ crystallographic structures, respectively.

The crystallographic structures of the samples were identified by comparing the results obtained with the crystallographic files deposited in the International Centre for Diffraction Data (ICDD) data base with the references #98-007-1506, #98-003-7822, and #98-001-3851 for monoclinic, hydrated orthorhombic, and hexagonal crystallographic structures of WO_3 , respectively, and #98-004-6169 for tungstic acid. To accomplish that, it was used the HighscorePlus PANalytical software.

Analysing Figure 6, it is possible to conclude that WN1 did not achieve the $m\text{-WO}_3$ crystallographic structure. Its diffractogram presents only two typical peaks of $m\text{-WO}_3$ (\diamond : 33.37° and 55.9°) while the others are characteristic of $\text{H}_2\text{WO}_4 \cdot n\text{H}_2\text{O}$ (\diamond), the intermediate product. Basically, the experimental conditions did not allow the total decomposition of $\text{H}_2\text{WO}_4 \cdot n\text{H}_2\text{O}$ once WN1 synthesis had a maximum duration of around 8 min and a temperature of only 100°C . For WN2 sample, all peaks were identified as characteristic of $o\text{-WO}_3 \cdot 0.33\text{H}_2\text{O}$. However, comparing with the respective crystallographic file, some peaks are absent in the diffractogram obtained, which means the $o\text{-WO}_3 \cdot 0.33\text{H}_2\text{O}$ crystallographic structure was not fully reached. Finally, the diffractogram of sample WN3 presents few perceptible peaks once the synthesis' conditions were not suitable and its yield was very low. However, the peaks that could be identified are characteristic of $h\text{-WO}_3$ crystallographic structure.

As the conditions of this programme were not suitable to obtain the desired crystallographic structures of WO_3 , another programme was tested: “Dynamic”. This programme allows a better control of the temperature during the synthesis as well as the time. Furthermore, with these modifications it was expected a greater yield for WN3 sample. Among tungsten trioxides, $h\text{-WO}_3$ is of particular interest once it is better suited for the transport of ions, which justifies the interest in the improvement of the WN3 sample. This feature is due to its open-tunnel structure that can act as an intercalation host for cations and electrons to form tungsten bronzes M_xWO_3 . [65]

The powders obtained using the “Dynamic” programme at different temperatures and times, are presented in Figure 7.

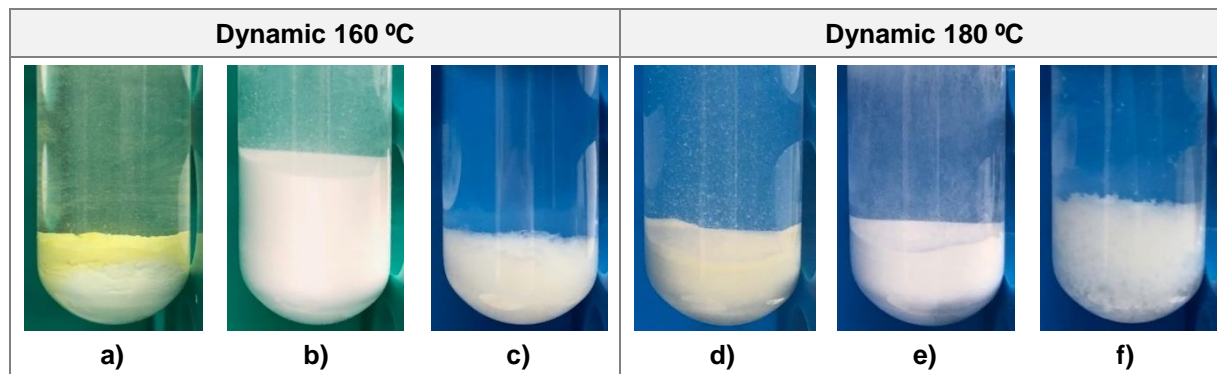


Figure 7: Powders obtained using the “Dynamic” programme at 160 °C during 40 min for a) WN1, b) WN2, and c) WN3; and at 180 °C during 1 h for d) WN1, e) WN2, and f) WN3. The vessels here presented have a maximum volume of 10 mL.

For the “Dynamic” programmes, all samples reached the time and temperature defined in the beginning of the synthesis. The sample with the highest yield at 160 °C was WN2, and WN1 at 180 °C. However, for each condition, the yields were very close for these two samples. The difference is that in Figure 7 b) the WN2 powder was not so compact as the one from WN1 (Figure 7 a)). Comparing the powder obtained for WN3 sample using this programme with the obtained using the aforementioned, it is noticeable an improvement, as desired. The aspect of the powders is equal to the aspect of the previous ones, with a slight difference related to the colour of WN1, which in Figure 5 b) was a strong yellow (“Fixed Power” 100 W) and became a pale yellow in “Dynamic” programme at 180 °C. To understand if this colour change is related with some modifications in the crystallographic structure of the sample, XRD analysis was performed, as well as for the other two samples. The results are presented in Figure 8.

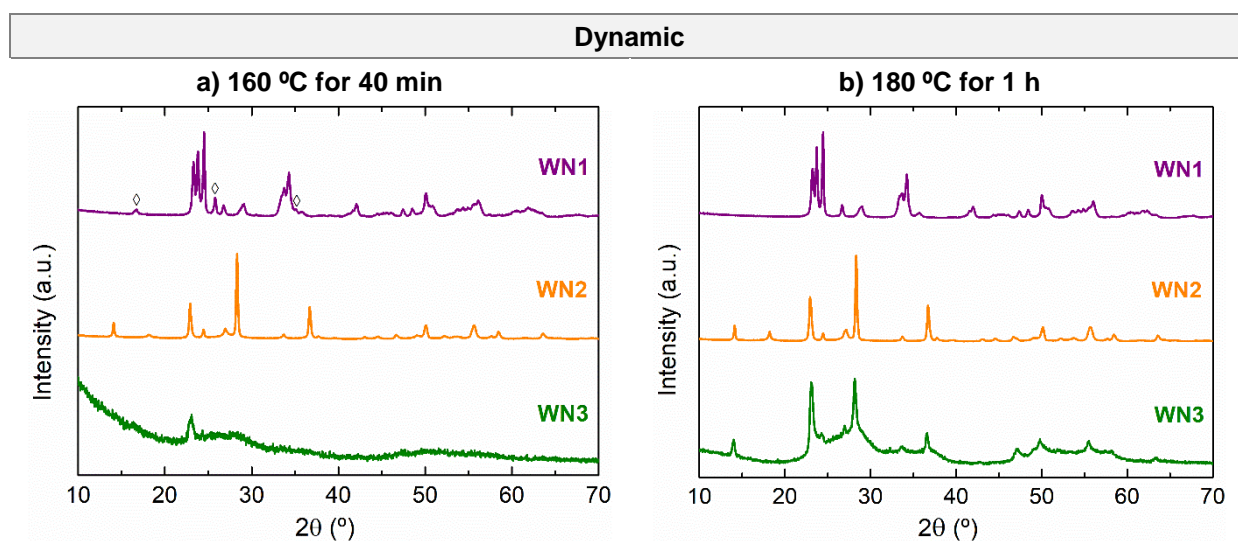


Figure 8: Diffractograms of the three WO_3 NPs samples produced by MAHS using the: a) “Dynamic” programme at 160 °C for 40 min; and d) “Dynamic” programme at 180 °C for 1 h. Peaks marked with \diamond are characteristic of $\text{H}_2\text{WO}_4 \cdot n\text{H}_2\text{O}$ crystallographic structure.

Analysing the diffractograms, it is possible to note some changes during the optimization process for each sample. The variation of the previously mentioned factors led to the achievement of the expected WO_3 crystallographic structures as well as their improvement: $m\text{-WO}_3$ (WN1), $o\text{-WO}_3 \cdot 0.33\text{H}_2\text{O}$ (WN2); and $h\text{-WO}_3$ (WN3). This supports the use of the “Dynamic” programme over the “Fixed Power” at 100 W.

All samples were produced using $\text{Na}_2\text{WO}_4 \cdot 2\text{H}_2\text{O}$ as a precursor, and NaCl (WN1 and WN2) or Na_2SO_4 (WN3) as a SDA. It is remarkable the influence of the sample’s pH in the crystallographic structure obtained, factor already studied by Marques et al. and previously mentioned. [51] The pH was the only difference between WN1 and WN2 (0.0 and 1.8, respectively) but it was enough to obtain different WO_3 crystallographic structures ($m\text{-WO}_3$ and $o\text{-WO}_3 \cdot 0.33\text{H}_2\text{O}$, respectively). Using Na_2SO_4 as SDA with a pH of 1.8, the WO_3 NPs grew with an $h\text{-WO}_3$ crystallographic structure.

In Figure 8 a), the diffractograms of the three samples produced using the “Dynamic” programme at 160 °C for 40 min are presented. For WN1, and comparing with the previous results, the improvement is noticeable since it was achieved the crystallographic structure of $m\text{-WO}_3$ (♦) with only three peaks that correspond to $\text{H}_2\text{WO}_4 \cdot n\text{H}_2\text{O}$ (◇: 16.56°, 25.7°, and 35.07°). In the diffractogram of WN2, it starts to appear a characteristic peak of $o\text{-WO}_3 \cdot 0.33\text{H}_2\text{O}$ crystallographic structure at around 18.08°, that was absent in the previous diffractogram (Figure 6). However, for WN3 these conditions are still not enough to reach the desired crystallographic structure of $h\text{-WO}_3$.

As already mentioned, the temperature and duration of the “Dynamic” programme were changed for 180 °C and 1 h, respectively, and the diffractograms obtained are in Figure 8 b). All peaks of WN1 diffractogram correspond to the crystallographic structure of $m\text{-WO}_3$ which means these conditions allowed the total decomposition of $\text{H}_2\text{WO}_4 \cdot n\text{H}_2\text{O}$. It is now possible to realize that the differences in the colour of this sample throughout the optimization process are related to the changes in its crystallographic structure. The strong yellow is characteristic of $\text{H}_2\text{WO}_4 \cdot n\text{H}_2\text{O}$ while the paler yellow is characteristic of $m\text{-WO}_3$. For WN2, all peaks are typical of $o\text{-WO}_3 \cdot 0.33\text{H}_2\text{O}$, and for WN3, the improvement is clear compared to the diffractograms of Figure 6 and Figure 8 a). WN3 peaks are all characteristic of $h\text{-WO}_3$.

In order to facilitate the perception of the optimization process for each sample (WN1, WN2, and WN3), all XRD analysis data presented is differently arranged in Figure 31 in section E of Appendices.

1.1.1. SEM analysis

The surface morphology of the samples produced via MAHS was analysed by SEM, and is presented in Figure 9. For the same precursor ($\text{Na}_2\text{WO}_4 \cdot 2\text{H}_2\text{O}$) three different morphologies were obtained: rectangular nanoplates assigned to $m\text{-WO}_3$ (WN1), nanosheets assigned to $o\text{-WO}_3 \cdot 0.33\text{H}_2\text{O}$ (WN2), and nanowires assigned to $h\text{-WO}_3$ (WN3).

According to XRD analysis, WN1 sample went through some changes in its crystallographic structure from $\text{H}_2\text{WO}_4 \cdot n\text{H}_2\text{O}$ to $m\text{-WO}_3$ (“Fixed Power” at 100 W to “Dynamic” at 180 °C for 1 h). This is confirmed by Figure 9. With the increment of synthesis’ temperature and time, the irregular nanoplates gradually transformed into completely rectangular nanoplates with sharp corners and smooth surfaces. Several clusters can also be seen. This increment also promoted the growth of WN3 sample nanowires, both in length and width, probably due to a slower nucleation. [64] It is also noticeable the formation of some clusters. Finally, for WN2 sample, there was also a morphological uniformization of the nanosheets throughout the MAHS optimization process.

It is also clear the influence of the SDAs (NaCl – WN1 and WN2, and Na_2SO_4 – WN3) in the morphology of the WO_3 NPs obtained, when the same precursor is used. The sulphate ions acted as capping agents by selectively binding to some crystal facets of the initial WO_3 crystal nuclei, covering them. For WN3, at pH 1.8, it is observed a faster growth rate along c-axis, leading to the formation of one-dimensional wire-like structures. Furthermore, a certain amount of sodium cations is required to stabilize the hexagonal and triangular tunnels in the formation of $h\text{-WO}_3$ in the sample. When chloride ions are used, instead of sulphate, it is believed that a similar process occurs, being the growth of the initial WO_3 crystal nuclei favoured in a specific direction. [51], [62] Compared to the other two morphologies, the unidimensional structure of $h\text{-WO}_3$ confers new and optimized characteristics to the material in terms of superficial area and physical properties like optical, magnetic and electronic ones.

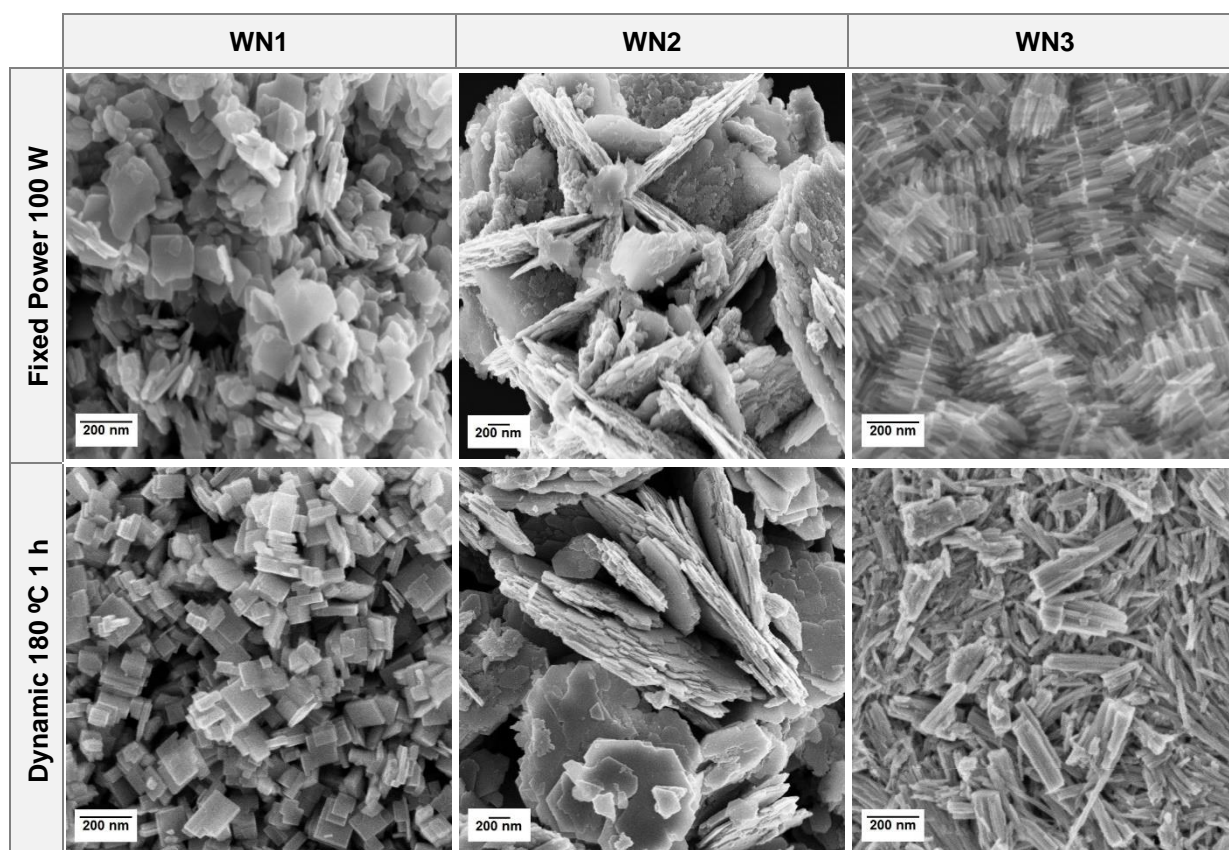


Figure 9: SEM images of the three different samples (WN1, WN2, and WN3) produced using the “Fixed Power” programme at 100 W, and using the “Dynamic” programme at 180 °C for 1 h.

The dimensions of the NPs obtained were also determined, using the software ImageJ. The results, concerning the length of the NPs, are presented in Table 3.

Table 3: Dimensions obtained for the WO_3 NPs produced by MAHS with the programmes “Fixed Power” at 100 W and “Dynamic” at 180 °C for 1 h, using the software ImageJ (n=40).

	NPs length (nm)	
	Fixed Power 100 W	Dynamic 180 °C 1 h
WN1	116 ± 44.3	107 ± 47.7
WN2	914 ± 270	826 ± 258
WN3	171 ± 41.6	350 ± 122

1.1.2. Raman spectroscopy

In order to complement the analysis performed, the crystal structure of the final three optimized WO_3 NPs samples produced by MAHS (WN1, WN2, and WN3) was also characterized by Raman spectroscopy. The normalized spectrum of each sample is presented in Figure 10.

The well-resolved peaks in the spectra indicates that all samples are crystalline. Crystalline WO_3 has three main spectral regions: one between 900 and 600 cm^{-1} , other between 400 and 200 cm^{-1} , and a third one below 200 cm^{-1} . Besides being characteristic of WO_3 material, the three regions correspond to stretching, bending, and lattice modes, respectively. [7], [57]

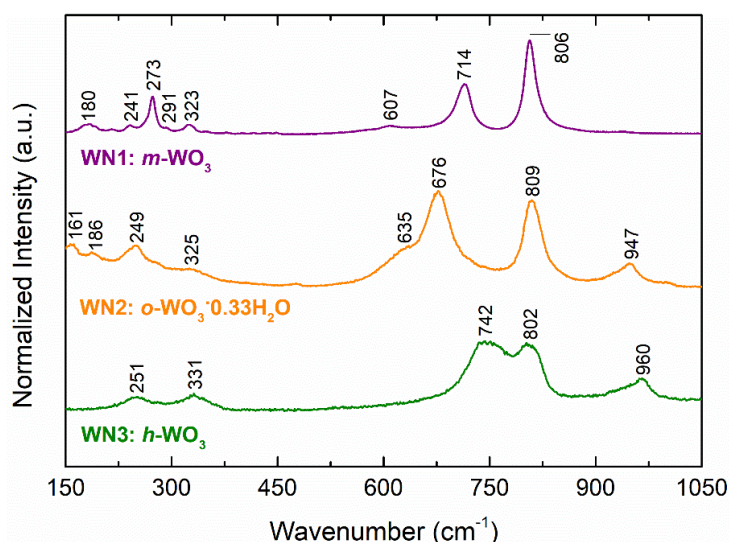


Figure 10: Raman spectra of WN1, WN2, and WN3 samples. The spectra were collected with a 633 nm laser, at 1% and 3 accumulations.

Starting with sample WN1, the Raman spectrum obtained is typical of *m*-WO₃. The two peaks with higher intensity, at wavenumbers of 806 and about 714 cm⁻¹, correspond to the stretching vibrations of O-W⁶⁺-O in octahedral WO₆. At 607 cm⁻¹ it is also observed a very weak peak, also related with stretching vibrations. Four weaker peaks at 323, 291, 273, and 241 cm⁻¹ are assigned to the bending vibrations of W⁶⁺-O-W⁶⁺ bond of corner oxygen. Finally, the peak at 180 cm⁻¹ is related to the lattice vibration. [7], [66]

In WN2 spectrum, the peak at wavenumber 947 cm⁻¹ corresponds to W⁶⁺=O bond and is related to the appearance of water between WO₆ octahedra layers. This is a typical peak for all types of WO₃ hydrates, proving that WN2 is also one. Water causes the distortion of WO₆ octahedron and promotes kind of a broadening of the peak at 635 cm⁻¹ which is related to the stretching vibration of W⁶⁺-O bond. Therefore, two peaks at 635 and 947 cm⁻¹ identify the appearance of water in WO₃ structure. At 809 and 676 cm⁻¹, WN2 presents two peaks that are specific for the W⁶⁺-O-W⁶⁺ bond stretching vibrations. Finally, at around 249 and 325 cm⁻¹, the peaks from O-W⁶⁺-O bending mode appear, and the ones below 200 cm⁻¹ (186 and 161 cm⁻¹) are related to the lattice vibration, as already seen. This Raman spectrum proves that WN2 is a sample of *o*-WO₃·0.33H₂O. [66]–[68]

In WN3 spectrum, the two peaks at 251 and 331 cm⁻¹ are assigned to the bending vibrations of the W⁶⁺-O-W⁶⁺ bridging oxygen. According to the literature, well defined peaks centered at around 260, 320, 650, 690, 786 and 810 cm⁻¹ can be assigned to *h*-WO₃ nanoparticles. However, the Raman spectrum of *h*-WO₃ nanowires is substantially different from that of the *h*-WO₃ nanoparticles. In the case of nanowires, it can be observed an overlapping of bands in the region between 600 and 850 cm⁻¹, and an exclusive terminal W=O stretching mode in the 925-965 cm⁻¹ interval that is normally related to all types of WO₃ hydrates. These two facts can be observed in WN3 spectrum: two peaks centered at 742 and 802 cm⁻¹, associated with the stretching vibration modes of O-W⁶⁺-O but with some overlap, and at 960 cm⁻¹, related to terminal W=O stretching mode. Although this last peak could also be related with the presence of water as a result of a poor drying process, the XRD analysis of the sample contradicts it. [62], [68]

The Raman spectroscopy data here presented supports the crystalline phases of each sample already established by XRD analysis, and confirms the high structural quality of WO₃ NPs produced by MAHS. In conclusion, it can be noticed that the resulting crystallographic structure and morphology of WO₃ NPs is dependent on synthesis' time, temperature, pH, and SDA.

1.2. WO₃ NPs by HS

In addition to MAHS, HS was also used to produce WO₃ NPs with *o*-WO₃·0.33H₂O crystallographic structure, as already mentioned. For this sample, the production process did not undergo through an optimization. However, it was also characterized by XRD and SEM, and later tested on the devices.

1.2.1. XRD analysis

In Figure 11, it is presented the diffractogram obtained for the WO_3 NPs sample produced by HS at $180\text{ }^\circ\text{C}$ for 1 h.

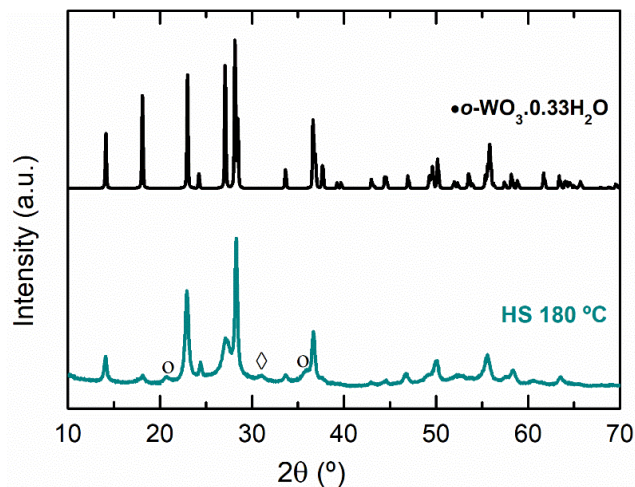


Figure 11: Diffractogram of WO_3 NPs sample produced by HS at $180\text{ }^\circ\text{C}$ for 1 h. The diffractogram represented in black is the crystallographic file deposited in the ICDD data base with the reference #98-003-7822 for hydrated orthorhombic crystallographic structure of WO_3 . Peaks marked with \diamond are characteristic of $\text{H}_2\text{WO}_4 \cdot n\text{H}_2\text{O}$ and peaks with \circ are non-identifiable.

The diffraction peaks observed are attributed to $\sigma\text{-WO}_3 \cdot 0.33\text{H}_2\text{O}$ with a mixture of a secondary product (\circ : 20.73° and 35.83°) not yet identified and $\text{H}_2\text{WO}_4 \cdot n\text{H}_2\text{O}$ (\diamond : 30.53°). These two additional peaks did not correspond to any file deposited in the ICDD data base and, basically, both are due to lattice distortions of the crystallographic structure during the slow growing of the NPs, as previously reported for WO_3 NPs produced by the same method. [6], [51]

1.2.2. SEM analysis

The SEM images of the sample produced by HS at $180\text{ }^\circ\text{C}$ for 1 h are presented in Figure 12. In this synthesis, it was not used an SDA and when this happens, the nanoparticles formed are of orthorhombic nature and aggregate to form a three-dimensional rectangular slab-like structure. [57] Analysing the images, the presence of two morphologies is very likely. One has bigger dimensions and a nanosheet/nanoplate structure while the other has smaller dimensions (around 15-25 nm), increasing the surface to volume ratio and providing more surface area for chemical and physical interactions. Comparing these results with the XRD analysis of this sample, the discrepancy of the NPs sizes can be associated with the presence of the intermediate product, $\text{H}_2\text{WO}_4 \cdot n\text{H}_2\text{O}$.

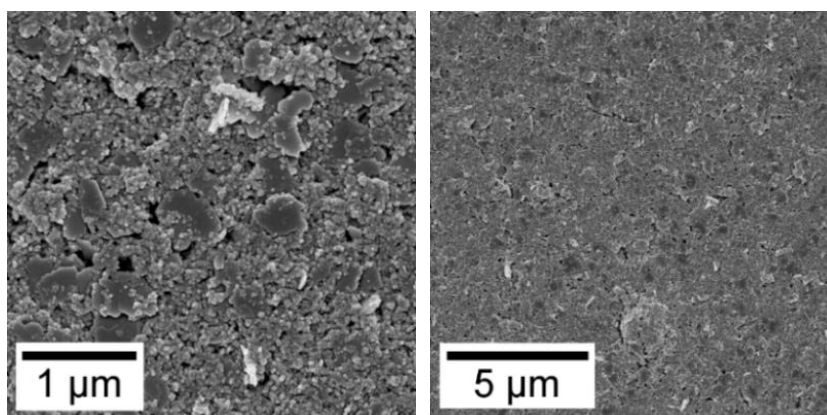


Figure 12: SEM images of the sample produced by HS at $180\text{ }^\circ\text{C}$ for 1 h, with different magnifications.

2. Devices' production

The devices obtained during the production process are presented in Figure 13.

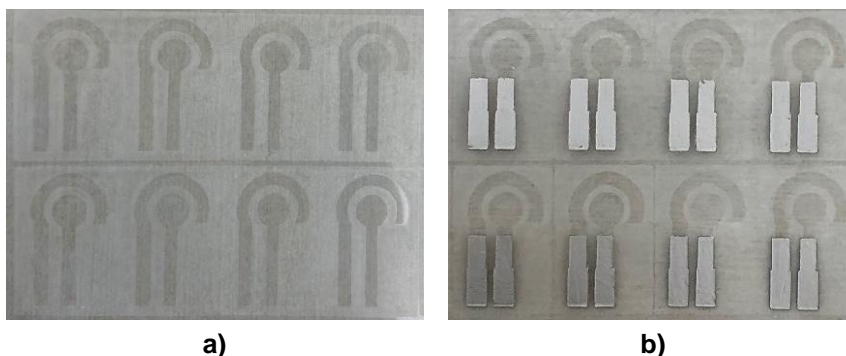


Figure 13: Devices obtained throughout the production process: a) after laser etching of ITO, and b) after deposition and curing of Ag ink.

The devices were designed in a 2-electrode system architecture and were negatively patterned in a single PET/ITO sheet by laser, in a mask less approach. For the laser etching of ITO, the laser-cutting machine took around 18 s for a single device, which was followed by the 3-step cleaning process of the PET/ITO sheet.

Before encapsulation, some devices were used to do preliminary tests described right after.

2.1. Preliminary tests

The first tests consisted in studying the deposition of the WO_3 NPs dispersion on the devices by drop-casting. The best conditions found were dropping a 2 μ L drop of the dispersion and letting it dry overnight. These conditions avoided the formation of the “coffee ring” effect and the late colouration of the WE centre, presented by drop-casting two drops (Figure 14 b)), and allowed a better uniformization of the deposited NPs, which did not happen when they were dried in a hot plate at 50 $^{\circ}$ C for 6 min (Figure 14 c)). After deposition, all devices were protected from light with aluminium foil, once WO_3 is also a photochromic material.

The WO_3 NPs dispersions were prepared by two methods: one was to grind and disperse the powders in a 1:1 mixture of EGBE and deionized water to achieve a concentration of 0.04 g/mL (Figure 14 a)) – method 1 –, and the other was to disperse the powders obtained right after the washing process in the same mixture and concentration – method 2. The concentration used was equal to all of the four WO_3 NPs samples (WN1, WN2, WN3 and HS 180 $^{\circ}$ C) to compare them later.

In order to choose the best method, some devices were tested using a typical electrolyte used in electrochromic windows: $LiClO_4$ 1 M dissolved in PC. The electrolyte was drop-casted right on top of the WE and CE, followed by an appliance of -3 V (explained in the devices' characterization) for 30 min, capturing the colour change of the NPs at 0, 5, 10, 20, and 30 min.

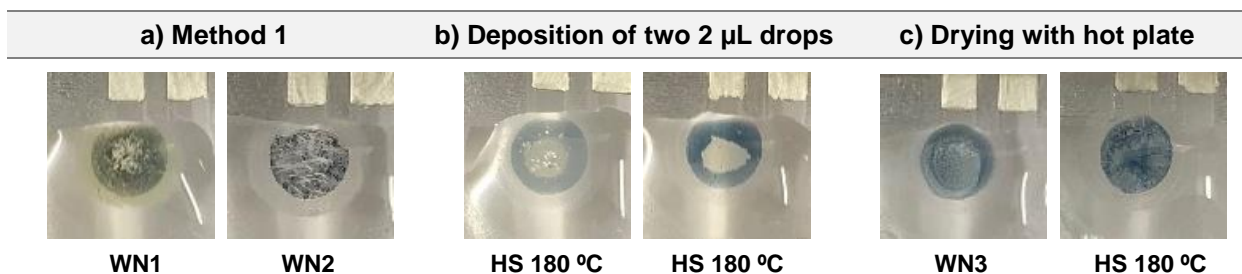


Figure 14: Observations during the preliminary tests of the devices before their encapsulation and after a colouration of 10 min. a) WO_3 NPs dispersion produced by method 1; b) Deposition of two 2 μ L drops of WO_3 NPs dispersion produced by method 2; c) Drying process using the hot plate of the WO_3 NPs dispersion produced by method 2.

All of the different WO_3 NPs dispersions produced by method 2 presented the same behaviour as the ones represented in Figure 14 b) and c), that only served to exemplify. After several tests, it was obvious that the dispersions produced by method 1 were not adequate because the powder grounded was not so

fine, compromising the WO_3 NPs dispersion and, consequently the colouration uniformity (Figure 14 a)). Thus, by using only the dispersions produced by method 2 and repeating the previous colouration tests, the WO_3 crystallographic structure that presented the most intense colour, to use later in the final devices, was found. The tests were repeated at least three times for each sample, being one of them presented in Figure 15.





















Sample	Time (min)				
	0	5	10	20	30
WN1					
WN2					
WN3					
HS 180 °C					

Figure 15: Colouration tests of the four deposited WO_3 NPs samples ($c=0.04$ g/mL) at an operating voltage of -3 V during 30 min.

Analysing Figure 15, it is possible to notice that every sample presented an electrochromic response visually detectable. This response is due to the formation of the tungsten bronze which presents a blue colouration. However, WN2 sample is the one that, for the same concentration of WO_3 NPs, presents the most intense colour for the electrolyte used. This sample corresponds to $\alpha\text{-WO}_3 \cdot 0.33\text{H}_2\text{O}$ produced by MAHS, and according to the literature it is a more conductive material because of the presence of double bonds and hydroxyl terminal groups. Due to its higher electronic conductivity and increased structure hydration, an enhancement in lithium ion diffusion rate, and hence faster electrochemical response, is expected. Also, WN1 ($m\text{-WO}_3$) can be excluded from further tests once its colour turns to a yellowish green and not in a uniform way, which can difficult the colour perception in the following tests. Besides, the electronic conductivity of stable WO_3 NPs was reported to be the highest for $\alpha\text{-WO}_3 \cdot 0.33\text{H}_2\text{O}$, as already mentioned, and gradually smaller for $m\text{-WO}_3$ and $h\text{-WO}_3$. [64], [69]

As the first conclusions were reached, the next step was to develop an electrolyte based on NaCl in order to simulate the human sweat. The electrolyte developed had to be liquid and non-aqueous to avoid the influence of the H^+ intercalation. Some solvents were studied (PC, and Acetonitrile) but for the NaCl concentrations used, only PG was able to dissolve the salt.

The same colouration tests were repeated for the devices with the WN2, WN3 and HS 180 °C NPs, using the new electrolyte (with a NaCl concentration of 60 mM), but this time with a colouration of only 6 min, once this time was sufficient to stabilize the colour and is more suitable for a rapid test. The colour change of the NPs was captured at 0, 1, 2, 4, and 6 min, and no colouration was observed for WN2 and HS 180 °C, as can be seen in Figure 16. For this reason, WN3 sample was the crystallographic structure chosen for the final devices. This fact is explained by the different size of the ions present in the two electrolytes, as well as the different openness degree of the studied WO_3 geometries. The ionic radii of Li (145 pm) is smaller than the one of Na (180 pm), and although the difference is small (35 pm), it is sufficient to the non-occurrence of Na^+ intercalation in the layered crystallographic structure of $\alpha\text{-WO}_3 \cdot 0.33\text{H}_2\text{O}$. [70], [71] For the $h\text{-WO}_3$ NPs, it was observed a colouration once its tunnel structure presents an openness degree higher than the structure of orthorhombic or monoclinic geometries. According to Sun et al., the theoretical intracrystalline tunnel size is 3.9 Å, which is more than sufficient to allow the intercalation of Na^+ , as well as other bigger cations to form tungsten bronzes. [51], [55]


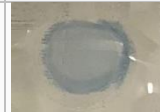

Time (min)	Sample (c=0.04 g/mL)		
	WN2	WN3	HS 180°C
6			

Figure 16: Colouration obtained at an operating voltage of -3 V during 6 min of the samples WN2, WN3 and HS 180 °C (c=0.04 g/mL) using the electrolyte composed by PG and NaCl at 60 mM.

In order to promote a faster ion transport, PEO and PVP were added to the electrolyte aforementioned, forming a sodium complexed electrolyte. In section D of Appendices, it is described the production process of this electrolyte. Also, to improve the intensity of the *h*-WO₃ NPs colouration, two other WO₃ NPs concentrations were studied: 0.06 and 0.08 g/mL. The results of the colouration tests for these concentrations, using the new electrolyte with a NaCl concentration of 60 mM, are presented in Figure 17.

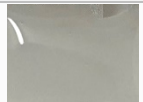
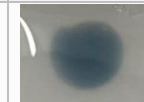
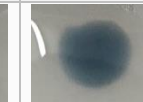
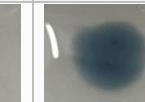
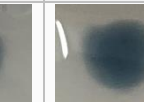

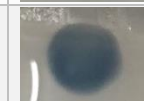



[WO ₃ NPs] (g/mL)	Time (min)				
	0	1	2	4	6
0.06					
0.08					

Figure 17: Colouration tests of the *h*-WO₃ NPs (c=0.06 g/mL and c=0.08 g/mL) at an operating voltage of -3 V during 6 min, using the electrolyte composed by PEO, PVP, PG, and NaCl at 60 mM.

Comparing these results with the ones obtained for WO₃ NPs concentration of 0.04 g/mL, the intensity of the blue is stronger. This is explained by the higher concentration of NPs used, as well as the sodium complexed electrolyte which promoted a faster ion transport.

As the best conditions related to the WO₃ NPs production, concentration and deposition were found, the next step was the encapsulation of the devices. For the definition of the hydrophilic paper pads and the patterning plus cutting of the plastic pouches, the laser-cutting machine took 5 s and 4.3 s, respectively, for a single device. The appearance of the devices after the deposition of the WO₃ NPs, as well as the final devices, is presented in Figure 18.

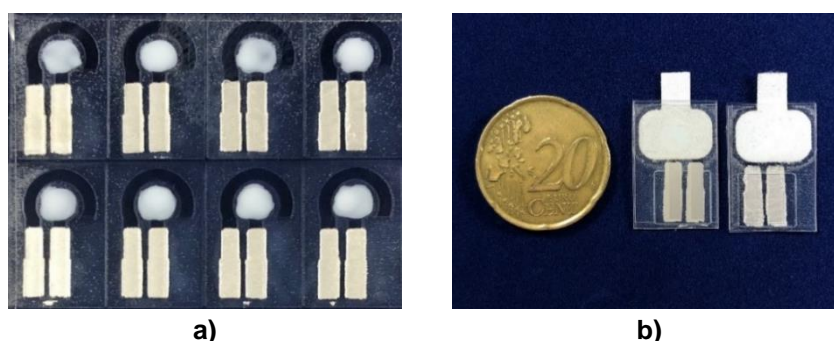


Figure 18: Appearance of: a) the devices after the deposition of the WO₃ NPs and before encapsulation; and b) the bottom and top view of the final devices.

The dimensions of the individualized final devices (Figure 18 b)) were around 1.4 x 2.0 cm. After the encapsulation, all devices were stored, protected from the light, and characterized. Also, the best concentration of the WO₃ NPs was then chosen.

3. Devices' characterization

The first characterization of the devices was concerning the effectiveness of the ITO etching by the laser-cutting machine. To accomplish that, it was performed an EDS analysis on a device, after the

deposition of the WO_3 NPs ($c=0.06$ g/mL) and before encapsulation. The device's area of interest was one that englobed both WE and CE, and the etched PET/ITO separation gap. In Figure 19 it is presented the analysis obtained.

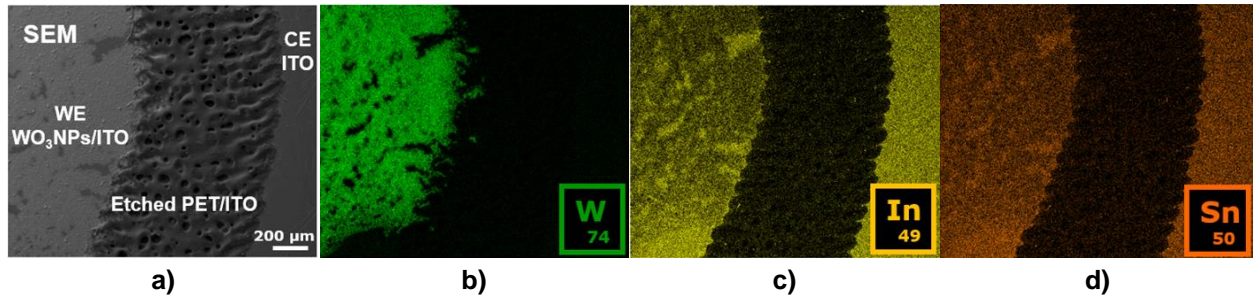


Figure 19: SEM (a) and EDS analysis (b, c), and d)) of the interface WE/etched PET/ITO area/ITO area/CE of a device with a WO_3 NPs concentration of 0.06 g/mL, before encapsulation.

The EDS analysis shows an effective ITO layer etching, once it is noticeable the absence of indium (In) and tin (Sn) on the etched areas between the electrodes. As such, laser method allows a fast, effective and high-resolution device patterning. Furthermore, it is a mask less method and allows freedom of design for the user. Confirmed the success of the devices production, a colourimetric analysis using the software ImageJ was carried out, before and after the devices' encapsulation.

3.1. Colourimetric analysis

The colouration tests previously described (Figure 17) were implemented to the devices with the two best WO_3 NPs concentrations (0.06 and 0.08 g/mL), during 6 min, using the electrolytes composed by PEO, PVP, PG, and all of the NaCl concentrations produced: 0, 30, 45, 60, 75, 90, and 120 mM. The goal was to find the concentration of NPs and the time that allowed a better distinction between the different NaCl concentrations.

Due to the planar structure of the device, the use of paper, and also the ITO colouration interference, the devices were not optically characterized by UV-vis in the transmittance mode. Besides, in practical terms, it is simpler to record the colouration obtained on the device with a cell phone camera, for example, and analyse its colour using a specific software, than measuring its transmittance. As such, an RGB analysis using the software ImageJ was carried out. This analysis gives the relative intensity of each RGB channel, which varies between 0 and 255, being all 0 when the colour is black and 255 when the colour is white. In this work, the intensity of the WE blue colour is of interest and to evaluate it, the ratios between the arithmetic means of the intensities obtained for the blue and red channels (B/R) were recorded. Ratios higher than 1 are considered positive for the blue colouration and ratios lower than 1 are considered negative. For each condition, three devices were tested, and the first analysis was performed on the devices before encapsulation. The results of the RGB analysis are presented in Figure 20.

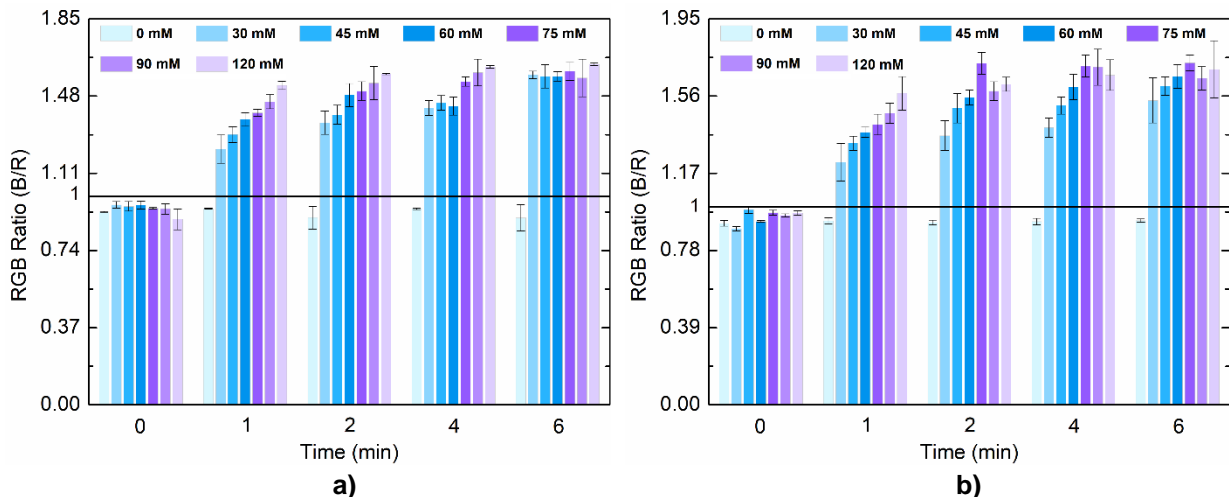


Figure 20: Results obtained from the RGB analysis of the devices before encapsulation, for a concentration of WO_3 NPS of: a) 0.06 g/mL; and b) 0.08 g/mL.

As expected, in both WO_3 NPs concentrations, for a colouration time of 0 min and a NaCl concentration of 0 mM, the B/R values are below 1 which indicates that there was no blue colouration of the NPs. For the other four times and NaCl concentrations, the B/R values are above 1, indicating the blue colouration of the NPs. Furthermore, it is noticeable that the ratio values are higher for the higher concentration of WO_3 NPs, 0.08 g/mL, which was also expected and visually seen.

By analysing Figure 20, the only conditions that allow a proper distinction between different NaCl concentrations are a colouration time of 1 and 2 min for a WO_3 NPs concentration of 0.06 g/mL and 1 min colouration for a WO_3 NPs concentration of 0.08 g/mL. For these conditions, the B/R values increase with the NaCl concentration rise in the electrolyte. Although not so obvious, the rest of the conditions also show the same behaviour, proving the existence of a relation between the intercalation of Na^+ in the $h\text{-WO}_3$ crystallographic structure and the intensity of the blue colouration presented by the NPs. This relation was already studied by De Matteis et al. [12], also in the development of a chromogenic device for CF diagnosis using a WO_3 film deposited by electron beam on a commercial ITO/glass substrate. However, and besides the positive results of their work, the research group only used concentrations of NaCl dissolved in Acetonitrile anhydrous of 0, 30, 60, and 90, and 120 mM.

To choose the best condition, the standard deviations had to be considered, and for a NPs concentration of 0.08 g/mL, in general, the values are higher. This can be explained by the ununiform NPs colouration for this concentration, due to the unnecessary number of NPs in the WE. The higher the concentration, the higher the time all NPs take to colouring, which translates into a ununiform colouration and an RGB analysis not so efficient nor reproducible. For these reasons, a WO_3 NPs concentration of 0.06 g/mL and a colouration time of 1 min was defined as the optimum condition for the CF diagnosis, presenting the following B/R values: 0.941 ± 0.001 for 0 mM, 1.226 ± 0.067 for 30 mM, 1.295 ± 0.039 for 45 mM, 1.368 ± 0.033 for 60 mM, 1.400 ± 0.018 for 75 mM, 1.453 ± 0.034 for 90 mM, and 1.531 ± 0.019 for 120 mM. The only downside of this colouration time is related with the standard deviations' overlap for NaCl concentrations of 30 and 45 mM, and also for 60 and 75 mM. However, these overlaps do not interfere with CF diagnosing, once non-affected individuals present a NaCl concentration in sweat lower than 30 mM, and CF patients present a NaCl concentration higher than 60 mM with an average of 80 mM.

The same analysis was performed on the devices after encapsulation and with a WO_3 NPs concentration of 0.06 g/mL, to compare with the previous results. For these devices, an electrolyte quantity of 60 μL , by excess, was drop-casted on the paper pads left outside each device. It took between 45 min and 1 h to cover all the area of the hydrophilic papers due to the viscosity of the electrolytes. The results of the analysis are presented in Figure 21.

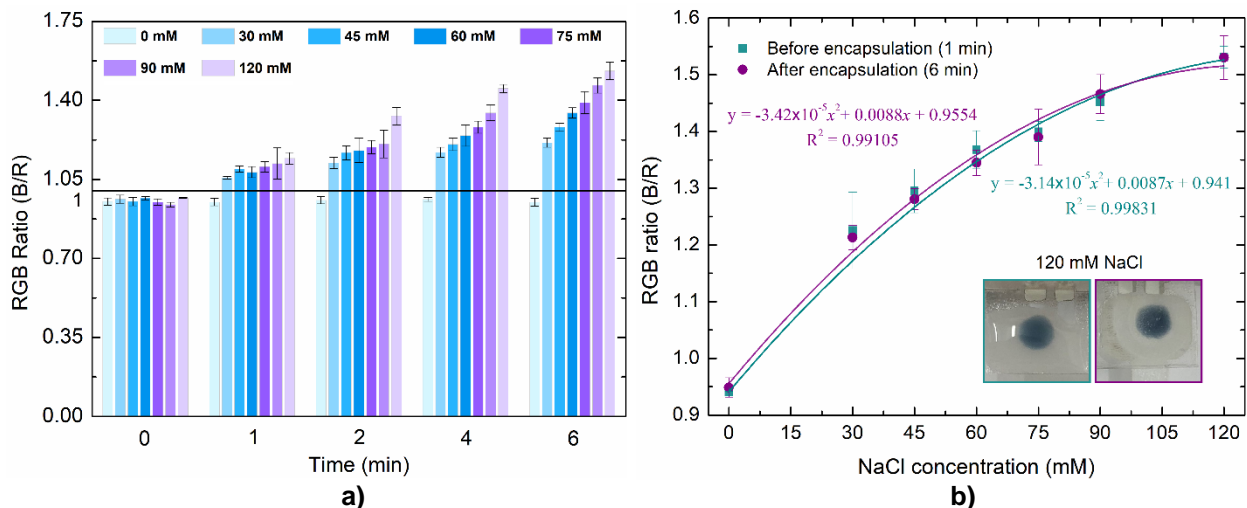


Figure 21: a) Results obtained from the RGB analysis of the devices after encapsulation, for a concentration of WO_3 NPs of 0.06 g/mL; and b) Comparison between the B/R values obtained for the devices with a concentration of WO_3 NPs of 0.06 g/mL before (1 min of colouration) and after (6 min of colouration) encapsulation, and respective calibration curves. Both images correspond to a device tested with the electrolyte containing 120 mM of NaCl before (left) and after (right) encapsulation.

After encapsulation, some previous features have remained. For a colouration time of 0 min and a NaCl concentration of 0 mM, the B/R values are below 1 (no NPs colouration) and for the rest, the values are above 1 (NPs colouration), as expected. Comparing these values with the previous obtained for the same WO_3 NPs concentration before encapsulation, the B/R values are very similar, although not significantly lower (Figure 21 b)). This is explained by the presence of the hydrophilic paper in the device, which can interfere with the colouration of the NPs when there are contact issues. If the paper soaked in the electrolyte is not in contact with the NPs, the NPs will not colour or will, but taking more time. This also explains the best colouration time found, which is 6 min. As such, the optimum condition for the CF diagnosis using the devices after encapsulation is a colouration time of 6 min for a WO_3 NPs concentration of 0.06 g/mL, presenting the following B/R values: 0.949 ± 0.017 for 0 mM, 1.213 ± 0.021 for 30 mM, 1.281 ± 0.018 for 45 mM, 1.345 ± 0.022 for 60 mM, 1.390 ± 0.049 for 75 mM, 1.466 ± 0.034 for 90 mM, and 1.530 ± 0.039 for 120 mM.

The results obtained and presented in Figure 20 and Figure 21, show that the developed devices can be used in the diagnosis of CF, after or before encapsulation with different optimum conditions. However, the human sweat presents other constituents beyond NaCl: K^+ , Mg^{2+} , H^+ , bicarbonate (HCO_3^-), etc. As such, to test the selectivity of the devices, some additional tests were performed.

3.1.1. Selectivity tests

Two more electrolytes were prepared, as described in section D of Appendices, with the maximum concentration of K^+ and Mg^{2+} found in sweat, as reported in literature: 10 and 2 mM, respectively. [12] The previous colouration tests were repeated on the devices with a WO_3 NPs concentration of 0.06 g/mL, before encapsulation, in order to test their selectivity. The images obtained during the colouration tests are presented in Figure 22.

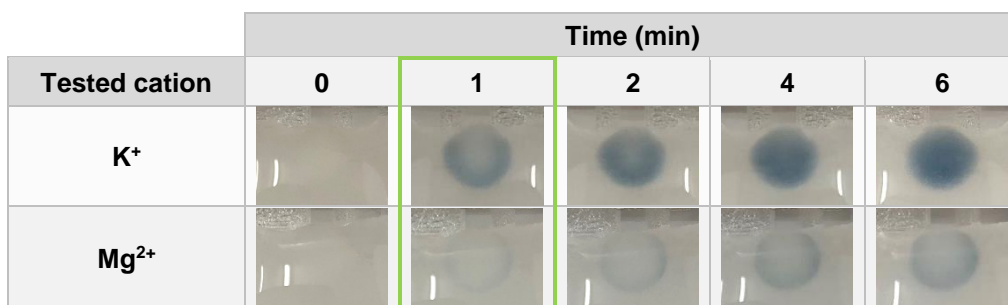


Figure 22: Colouration tests of the final devices, before encapsulation, with a WO_3 NPs concentration of 0.06 g/mL, at an operating voltage of -3 V during 6 min, using two electrolytes: one composed by PEO, PVP, PG, and KCl (10 mM), and other by PEO, PVP, PG, and MgO_4S (2 mM).

For each electrolyte, three devices were tested and all have shown colour intensities similar to the ones presented in Figure 22. As also observed by De Matteis et al. [12], the colouration obtained for the KCl electrolyte is more intense than the obtained for the MgO_4S electrolyte, which is almost inexistent. This is explained by the difference between ion concentrations. For 1 min of colouration, the best time found for the devices before encapsulation, the blue intensity for KCl is considerable.

With this in count, a third electrolyte composed by KCl, MgO_4S , and NaCl at 0, 30, 60, and 120 mM, was prepared and also tested. An RGB analysis for this last electrolyte was performed. The goal was to study if the relation between the blue intensity of the NPs and the concentration of NaCl remained, as an electrolyte more similar to human sweat was approached. The results for a colouration time of 1 min are shown in Figure 23.

As can be noticed, a relation between the blue intensity of the NPs and the concentration of NaCl remains, which proves the reliability of the device developed even with the influence of other ions as happens in human sweat. It is noteworthy that in this case, a B/R value higher than 1 is obtained for a NaCl concentration of 0 mM due to the contribution of the other ions present in the electrolyte.

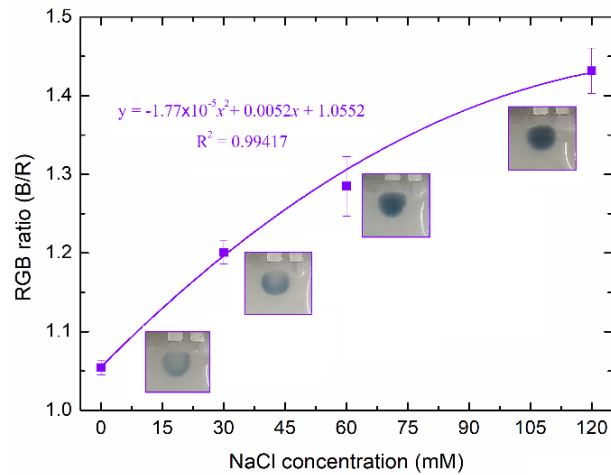


Figure 23: Calibration curve obtained with the B/R values of the colouration tests (1 min) performed on the devices before encapsulation, with a concentration of WO_3 NPs of 0.06 g/mL, and using the electrolyte composed by PEO, PVP, PG, NaCl, KCl, and MgO_4S .

As the functionality of the device was evidenced, the next stage was its electrochemical characterization.

3.2. Electrochemical characterization

The structural openness makes $h\text{-WO}_3$ an interesting system to understand the structure-property relationship during electrochemical cycles, where charge transfer processes are usually involved. Although not presenting a practical contribution for the application here developed, the electrochemical response of the deposited $h\text{-WO}_3$ NPs on the devices after and before encapsulation was evaluated by cyclic voltammetry, using the electrolyte composed by PEO, PVP, PG, and NaCl at 60 mM as the supporting electrolyte (Figure 24). The contact area between the electrolyte and the NPs was 0,785 cm^2 , and 10 cycles were performed from 3 to -3 V, as this was the applied potential during the previous tests, at a scan rate of 100 mV/s for specific colouration/bleaching cycles. It is noteworthy that during each cycle, the colour of the NPs was observed to change from blue to a whitish-blue, reversibly.

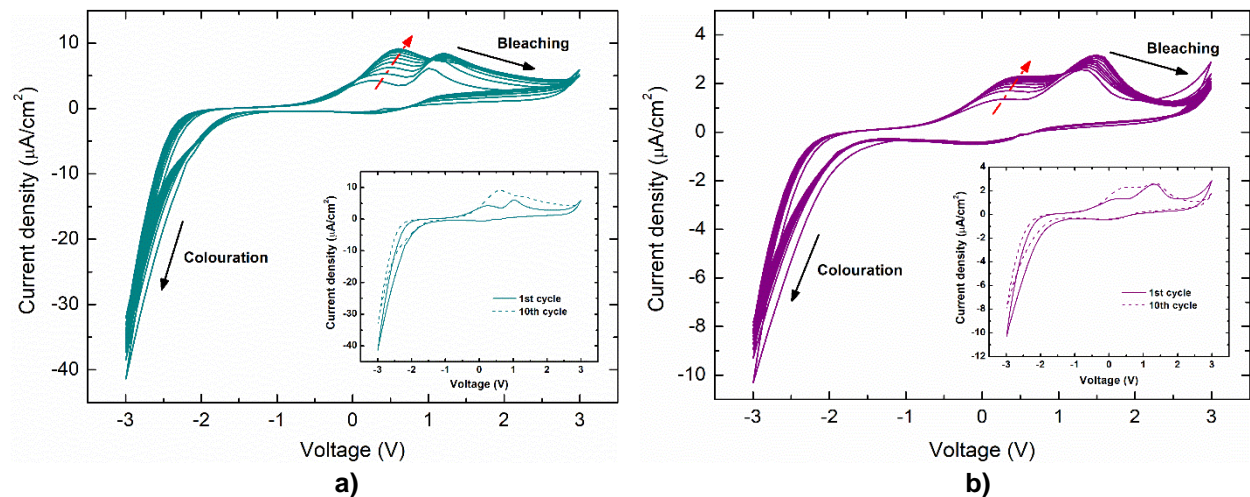


Figure 24: Cyclic voltammetry curves obtained for the devices a) before and b) after encapsulation. The measurement was performed using the electrolyte composed by PEO, PVP, PG, and NaCl at 60 mM, from 3 to -3 V at a scan rate of 100 mV/s, during 10 cycles.

Comparing Figure 24 a) and b), the current density obtained for the device before encapsulation is higher than the obtained for the device after encapsulation. This fact can be related with the contact area between the electrolyte and the NPs, which is higher for the device before encapsulation once the electrolyte is drop-casted directly on the NPs, allowing its spread through all interstitial spaces between NPs. On the contrary, in the devices after encapsulation, the electrolyte is more concentrated on the NPs surface, as the paper pad is the vehicle for its propagation. Even if the same quantity of electrolyte is drop-

casted on both devices, the amount that reaches the NPs will be different. Furthermore, when the contact area is bigger, it can be seen that the area between the curves also increases which is associated with more electro-reducible sites, thus experiencing higher charge insertion. These facts also explain the difference between the colouration tests' time for both devices, being 1 min for the ones before encapsulation and 6 min for the ones after encapsulation.

The developed devices were designed for a disposable colourimetric analysis with no need for a bleaching step. However, both colouring and bleaching steps were studied. As already mentioned, WO_3 exhibits a cathodic colouration which is connected to the insertion of both electrons and charge compensation ions for colouration (negative voltages) and the opposite mechanism for bleaching (positive voltages). As such, by analysing Figure 24, both reduction (colouration) and oxidation (bleaching) peaks can be observed. An interesting behavior can be observed for both Figure 24 a) and b). While the reduction peak remains almost equal throughout the 10 cycles, the one concerning the WO_3 oxidation appear as two peaks that throughout the cycles merge into one at higher currents, stabilizing. Few research groups used NaCl-based electrolytes for WO_3 applications, and the ones who used did not perform cyclic voltammetry analysis or used different production and deposition techniques [12], [55]. As such, several factors can be influencing the oxidation step of WO_3 . Sun et al. [55], studied the influence of the absorption of three different cations, Na^+ included, on the stability of $h\text{-WO}_3$ tunnels. The research group concluded that due to the larger size of this cation, compared to Li^+ and H^+ , it induces a phase transformation in $h\text{-WO}_3$. Also, they observed some changes in the electrochemical behavior of $h\text{-WO}_3$ for the different electrolytes. With this in mind, structural deformations can be in fact happening, and the applied voltage can also be contributing for it. To test this assumption, similar additional tests were performed on the devices before encapsulation, by only changing the applied voltages to -2.5 V to 3 V and the number of cycles to 4. The results are presented in section F of Appendices. As can be seen in Figure 32 d), with the application of only -2.5 V, the cyclic voltammetry curves present a totally different behavior, presenting only one oxidation peak centered at around 0.3 V. As such, it is possible to conclude that when applying -3 V, the structure of $h\text{-WO}_3$ can be somehow rearranged into other, altering the ions' deintercalation process, stabilizing the rearrangement with the number of cycles. When only applying -2.5 V, this process does not occur. Other factor that can also be associated with the obtention of these peaks is the deterioration of the process' reversibility. Some ions can be trapped in the crystallographic structure of $h\text{-WO}_3$ and/or need higher voltages to leave the structure in the bleaching step, which can justify the shift observed in the oxidation voltages. When applying -2.5 V, the same does not happen, and the oxidation peak barely changes. Finally, the electrochromic behavior of ITO can also be interfering with the process. [72] However, to have certainty of these assumptions, additional tests need to be performed.

With the number of cycles, it was observed that both coloured and bleached states were affected, fact that is associated mainly to trapped charges (Na^+), unable to exit the material, and that can be observed in Figure 25 for the device before encapsulation.

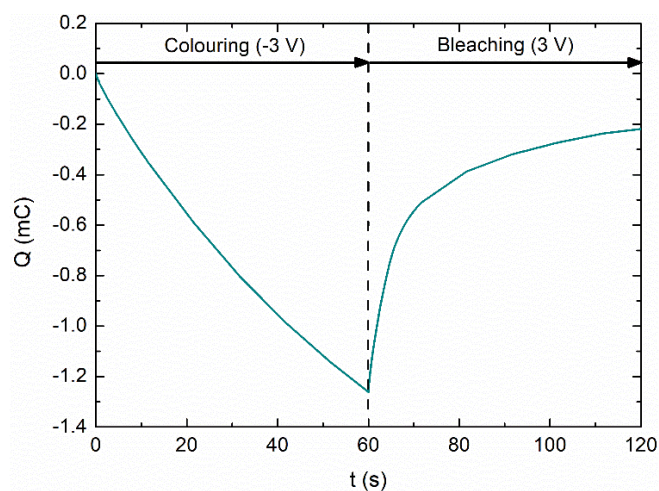


Figure 25: Charge insertion and extraction during consecutive 120 seconds colouration (-3 V) and bleaching (3 V) during the first cycle for the device before encapsulation.

Chronocoulometry is the measurement of charge per unit of time. As such, the experiment starts at a potential where no reaction is occurring and stepped instantaneously to a potential where either the oxidation or reduction occurs. As can be seen, inserted charges after 60 seconds of colouring do not equal the extracted charges after the bleaching step, presenting a charge balance less than 1 that is the optimum value for a durable material. Furthermore, the degradation of the electrolyte can also influence its ability to provide sodium ions for the electrochromic reactions to occur, once organic electrolytes are more susceptible to experience degradation. As such, this degradation can also affect the material colour stability.

Cyclic voltammetry analysis was also performed at different scan rates (25, 50, 75, 100, and 125 mV/s) between -3 and 3 V, for the device before encapsulation. The curves are shown in Figure 26.

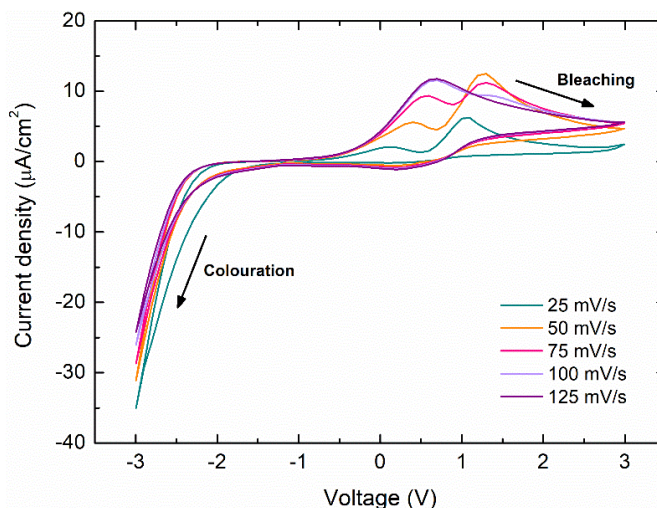


Figure 26: Cyclic voltammetry curves obtained for the device before encapsulation between -3 and 3 V at different scan rates: 25, 50, 75, 100, and 125 mV/s. The measurement was performed using the electrolyte composed by PEO, PVP, PG, and NaCl at 60 mM.

As can be seen, the peak current, associated to the Na^+ deintercalation, increases accordingly with the scan rate increasing, and also shifts towards the positive potential. For scan rates equal or higher than 100 mV/s, the peak tends to stabilize. This reveals that the anodic peak current is linearly proportional to the square root of scan rate, which suggests a process that is diffusion controlled. [47], [73] Concerning the cathodic peak, it is more difficult to deduce due to its low prominence.

The same behavior presented in Figure 24 can also be observed in Figure 26: the appearing of two peaks in the bleaching stage. However, for a scan rate of 125 mV/s these peaks are already merged. Comparing the first cycle at 100 mV/s (Figure 24) with the first cycle at 25 mV/s (Figure 26), these two peaks are more prominent at the lowest scan rate, as expected, once the analysis takes more time. Once more, similar additional tests were performed on the devices before encapsulation, by only changing the applied voltages to -2.5 V to 3 V and the number of cycles to 4 for each scan rate: 25, 50, 75, 100, and 125 mV/s. The results are presented in section F of Appendices, and as already observed, for this potential range, the appearing of two peaks does not occur.

3.3. Final device

The CF diagnostic device here proposed was successfully developed. The disposable colourimetric WO_3 -based device represents a low-cost candidate for POC diagnostic applications, especially in resource-limited environments, once it was produced with cost-effective and simpler methods: MAHS for the WO_3 NPs production, and laser technique for ITO etching of the PET/ITO sheet. While MAHS provides a total control over the shape and size of the NPs with a low temperature process, the laser technique offers a fast and high-resolution device patterning allied to a freedom of design for the user.

It is noteworthy that this device is based on sweat Na^+ concentrations measurement. Compared to other devices that measure NaCl concentrations, the one here proposed is more accurate since it has higher selectivity for Na^+ due to this cation intercalation on the crystallographic structure of $h\text{-WO}_3$. Although Na^+ concentration in sweat is elevated in CF patients, the current CFF guidelines recognize that its

determination is less discriminatory when compared to Cl⁻. [15] However, multiple studies identify the reliability of using Na⁺ for CF detection, and even recommend the use of both to avoid diagnostic errors. [12], [74], [75] Nevertheless, Cl⁻ or Na⁺ values greater than 60 mmol/L are consistent with the diagnosis of CF. [76]

In Figure 27 is presented the final apparatus needed for the use of the device in the diagnosis of CF.

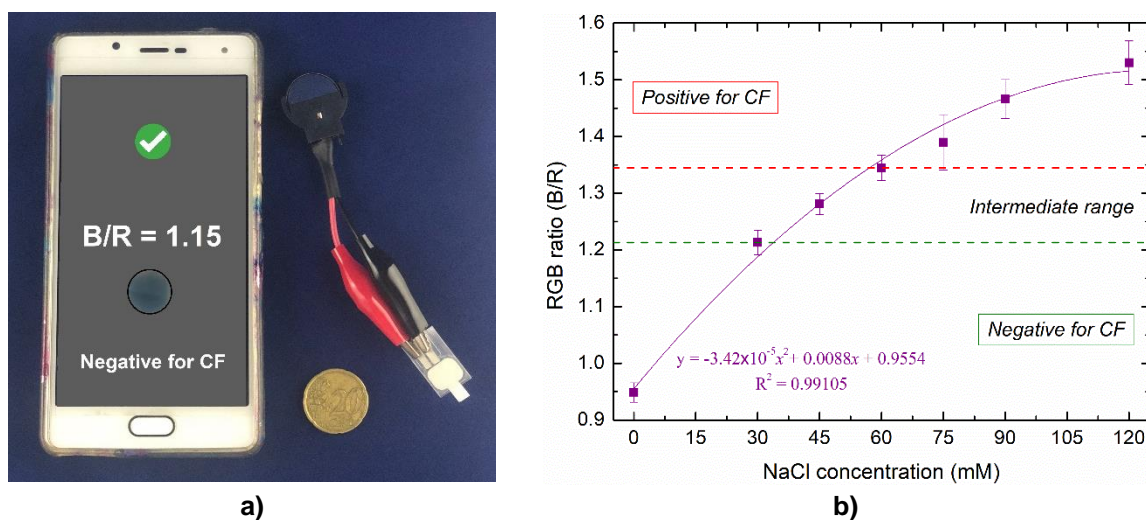


Figure 27: Final apparatus needed for the use of the device in the diagnosis of CF: a) a 3 V battery connected to the device and a cell phone for recording the colouration presented by the device after usage; b) calibration curve obtained with the B/R values of the devices after encapsulation with a WO₃ NPs concentration of 0.06 g/mL and a colouration time of 6 min using the electrolyte composed by PEO, PVP, PG and NaCl. The dashed lines represent the B/R values correspondent to the NaCl concentration of 30 and 60 mM, that indicate a negative and positive diagnosis for CF, respectively.

As already mentioned, this device can be used in two different stages, both with different advantages: before or after encapsulation. For both options, Wescor Macroduct® sweat collection system can be used, which includes sweat stimulation by pilocarpine iontophoresis for 5 min, and sweat collection in a plastic coil placed over the iontophoretically-stimulated area on the skin. [15] If the user chooses to use the developed device before encapsulation, the collected sweat can be drop-casted directly on the WE. If not, by using the device after encapsulation, the collected sweat can also be drop-casted on the paper pad, waiting till it covers the WE (between 45-60 min for 60 μL of the electrolyte tested), or the device can be placed directly over the iontophoretically-stimulated area on the skin, using a medical dressing to attach it on the skin. This way, the stimulated sweat goes directly to the paper pad. This is the main advantage of the proposed device compared to other electrochromic devices: instead of having a typical electrochromic device structure with an electrolyte layer, the electrolyte is drop-casted on the WE only on time of usage, which eliminates leakage problems.

After the drop-casting of the electrolyte, an operational voltage of -3 V is applied to the device during 1 or 6 min if using the device before or after encapsulation, respectively. This voltage can be provided using a power supply as the one used in this work, a 3 V battery as represented in Figure 27 a), or even using the power from the cell phone. The colour intensity obtained is then recorded with a cell phone camera for further RGB analysis using a proper software. Depending on the option chosen, the B/R values correspondent to a negative and a positive diagnosis for CF are different. In Figure 27 b), the calibration curve represented corresponds to the B/R values obtained for the device after encapsulation, with a colouration time of 6 min using the electrolyte composed by PEO, PVP, PG, and NaCl. For this case, a negative result for CF is found for B/R values smaller than 1.213 ± 0.021 (30 mM of NaCl) and a positive result for B/R values equal or higher than 1.345 ± 0.022 (60 mM of NaCl). In case of using the device before encapsulation, a positive diagnosis is obtained for B/R values equal or higher than 1.368 ± 0.033 (60 mM of NaCl) and a negative diagnosis for B/R values smaller than 1.226 ± 0.067 (30 mM of NaCl). If the B/R value obtained is between these two limits, in the intermediate range, the examined person must perform additional tests to better evaluate its condition.

The developed device was tested using different NaCl-based electrolytes that deviate from the real constitution of human sweat. Although a more complex electrolyte was tested during the selectivity tests,

with very satisfactory results, human sweat presents several more constituents, including water. De Matteis et al. [12] opted to evaporate the human sweat sample to avoid the intercalation of H⁺. The same can be applied to this device: the water can be evaporated and the remaining salt can be dissolved in the developed solvent (PEO, PVP and PG), proceeding with the rest of the process.

As already mentioned, an early diagnosis of CF facilitates early implementation of therapy, which can significantly improve the prognosis and life quality of the affected patients. However, according to a survey undertaken by the European Cystic Fibrosis Society back in 2017, in Europe, the cost of a sweat test can vary between 20-300 €. [4] In contrast, and as discriminated in Table 4, the device here developed has a cost of only 13 cents (0.128 €). This analysis does not include the costs related with the electricity of the equipment used (microwave, oven, laser machine, centrifuge, desiccator, ultrasonic bath and hot plate).

Table 4: Costs analysis of the developed device.

Material	Quantity	Cost	Cost/device (€)
PET/ITO sheet	30.5 cm × 30.5 cm × 127 μm	29 €/sheet	8.63×10 ⁻²
Laminating pouches	9.9 cm × 6.7 cm × 125 μm	0.12 €/pouch	4×10 ⁻²
Paper Whatman n.º4	46 cm × 57 cm × 205 μm	2.18 €/sheet	1.15×10 ⁻³
<i>h</i>-WO₃ NPs	0.12 mg	8.03×10 ⁻³ €/mg	9.64×10 ⁻⁴
Total:			0.128 €

Chapter IV: Conclusions and Future Perspectives

The aim of this work was the development of an electrochromic POC device, based on WO_3 NPs, for a facile diagnosis of CF especially in resource-limited environments. The synthesis of the NPs was performed by HS and MAHS. The ones produced by MAHS went through an optimization process that consisted in the variation of microwave programme, synthesis' temperature, pressure, power, and time, to achieve three crystallographic structures: $m\text{-WO}_3$ (WN1); $\alpha\text{-WO}_3 \cdot 0.33\text{H}_2\text{O}$ (WN2); and $h\text{-WO}_3$ (WN3).

The optimization process of the WO_3 NPs synthesis through MAHS was successful, being the last programme tested (Dynamic 180 °C for 1 h with a maximum power of 200 W) the one with the best conditions to reach the desired crystallographic structures, analysed by XRD analysis, and also greater yields, especially for WN3. The "Dynamic" programme allowed a better control of temperature and time during synthesis, leading to the achievement of products with no impurities. In order to complement this study, and also to improve the crystallographic structure of all samples, especially WN3 and its yield, a temperature of 200 °C during 40 min, for example, could be tested.

Raman spectroscopy proved to be an excellent auxiliary technique to XRD analysis since it confirmed the crystalline phases of the samples after the optimization process. SEM analysis allowed to study the morphology of all samples and also to analyse the dimensions of the NPs obtained. For WN1 sample, rectangular nanoplates were obtained with a medium length of 107 ± 47.7 nm. For WN2, nanosheets were obtained (medium length of 826 ± 258 nm) and for WN3 nanowires with a medium length of 350 ± 122 nm. Throughout this analysis, it was possible to notice that the resulting crystallographic structure and morphology of the WO_3 NPs produced are dependent on synthesis' time, temperature, pH, and SDA. The same precursor ($\text{Na}_2\text{WO}_4 \cdot 2\text{H}_2\text{O}$) was used in all samples, being the WN3 sample's SDA (Na_2SO_4) different from WN1 and WN2 samples' SDA (NaCl). For WN3, the sulphate ions acted as capping agents by covering some crystal facets of the initial WO_3 crystal nuclei, promoting a faster growth rate along c-axis. When chloride ions are used it is believed that a similar process occurs. However, the growth of the initial WO_3 crystal nuclei is favored in a different specific direction, as observed in the data. [51], [62]

In conclusion, it was evidenced that MAHS is a method capable to produce NPs with high structural quality with a lower power consumption and faster reaction times.

Concerning the sample produced through HS at a temperature of 180 °C during 1 h, all XRD peaks were identified as characteristic of $\alpha\text{-WO}_3 \cdot 0.33\text{H}_2\text{O}$ except for three additional peaks. One was related to the presence of $\text{H}_2\text{WO}_4 \cdot n\text{H}_2\text{O}$ in the sample, while the other two were already reported as characteristic of lattice distortions in the crystallographic structure of WO_3 NPs while being formed. Through the analysis of its SEM image, this sample seemed to present two types of NPs, probably associated with the presence of $\text{H}_2\text{WO}_4 \cdot n\text{H}_2\text{O}$: one with bigger dimensions and a nanosheet/nanoplate structure, and the other with smaller dimensions (around 15-25 nm). It is noteworthy that this sample did not go through any optimization process, so as a future perspective it could be done.

After the NPs' synthesis, the fabrication of the devices and the realization of some preliminary tests took place. As mentioned, a CO_2 laser technology was used in the devices' production, which saved time and costs. It only took 27.3 s for the production of each device (ITO etching, cutting the hydrophilic paper pads and patterning plus cutting of the plastic pouches), which presented a final dimension of around 1.4 x 2.0 cm. In the preliminary tests it was found that a 2 μL drop of the NPs' dispersion followed by a natural drying overnight were the best conditions to produce the devices. The drop-casting step was of great importance to obtain a good uniformization of the deposited NPs, as well as a later uniform colouration. In fact, as a future perspective, screen printing technique could also be tested to find the one that allows the best NPs' uniformization.

For the colouration tests, an electrolyte based on PEO, PVP, PG, and NaCl at different concentrations (0, 30, 45, 60, 75, 90, and 120 mM) was developed to simulate the human sweat. The tests were performed on the devices during 30 min at an operating voltage of -3 V, and WN3 was the only sample that showed a colouration, fact explained by the tunnel structure of $h\text{-WO}_3$ that allowed the intercalation of Na^+ . As such, WN3 was the WO_3 crystallographic structure chosen for the final devices, with a dispersion concentration of 0.06 and 0.08 g/mL.

The next step was the proof of concept with the diagnosis of CF and, for that, colouration tests were performed during 6 min at -3 V on the devices with the two above mentioned NPs concentrations, before the devices' encapsulation. Due to their planar structure, the use of paper, and also the ITO colouration

interference, the devices were not optically characterized by UV-vis in the transmittance mode. Instead, the comparison between the blue colouration intensities was analysed by an RGB analysis, using ImageJ software, and the ratio of the average intensities in blue and red channels was calculated. The devices with a WO_3 NPs concentration of 0.06 g/mL allowed the best distinction between the different NaCl concentrations, for a colouration time of 1 min, compared to the concentration of 0.08 g/mL. The B/R values obtained for each NaCl concentration were: 0.941 ± 0.001 for 0 mM, 1.226 ± 0.067 for 30 mM, 1.295 ± 0.039 for 45 mM, 1.368 ± 0.033 for 60 mM, 1.400 ± 0.017 for 75 mM, 1.453 ± 0.034 for 90 mM, and 1.531 ± 0.019 for 120 mM. After encapsulation, the best time of colouration was 6 min. However, the B/R values obtained were smaller due to the presence of the paper pad, which can interfere with the colouration of the NPs when there are contact issues. The B/R values obtained were: 0.949 ± 0.017 for 0 mM, 1.213 ± 0.021 for 30 mM, 1.281 ± 0.018 for 45 mM, 1.345 ± 0.022 for 60 mM, 1.390 ± 0.049 for 75 mM, 1.466 ± 0.034 for 90 mM, and 1.530 ± 0.039 for 120 mM.

Selectivity tests were also performed to study the influence of common interferents in sweat (Mg^{2+} and K^+) in the colouration of the devices. It was obtained a colouration for both, but the one obtained for the KCl electrolyte was more intense than for the MgO_4S electrolyte, fact explained by the difference between ion concentrations. However, a relation between the blue intensity of the NPs and the concentration of NaCl remained, which proved the reliability of the device developed even with the influence of other ions.

Although the devices here developed were designed for a disposable colourimetric analysis, an electrochemical characterization was performed by cyclic voltammetry and chronocoulometry. Both reduction and oxidation peaks were observed and an interesting behaviour concerning the bleaching step occurred. While the reduction peak remained almost equal throughout 10 cycles, at a scan rate of 100 mV/s, the one concerning the WO_3 oxidation appeared as two peaks that throughout the cycles merged into one at higher currents, stabilizing. Several factors can be influencing the oxidation step of WO_3 like the electrochromic behaviour of ITO, the deterioration of the process' reversibility, and the applied voltage (-3 V) that can be inducing a phase transformation in the $h\text{-WO}_3$, as already reported elsewhere. [55] However, additional tests need to be implemented to have certainty of these assumptions, like an XRD analysis before and after the colouration step of the devices.

Some studies are still needed to characterize the electrolytes produced. XRD analysis could be used to investigate the semi-crystalline nature of the PEO/PVP blend, the influence of NaCl addition on the polymer blend crystallinity, and also to confirm the dissolution of the salts. FTIR analysis could confirm the complexation of the salt used with the polymer host, and could also indicate if there was a good miscibility between PEO and PVP. The electrical conduction mechanism in the blend could also be studied to complete the characterization. [46] Furthermore, different solvents could be studied and tested in order to reduce the viscosity of the electrolyte developed here. This way, it would be possible to reduce the time that the electrolyte takes to cover the paper pad of the devices after encapsulation. Also, electrolytes with a composition more similar to human sweat or even real human sweat could be tested. The B/R values obtained could then be compared with the results from a more precise and CFF accepted technique, as coulometry. In addition, durability tests could be performed to study the stability of the devices throughout the time, for both before and after encapsulation. Related with the devices after encapsulation, a study concerning the use of different types of paper could also be done, in order to study the influence of the paper pad porosity in the NPs colouration or just in the time that the electrolyte takes to completely cover it.

Concluding, the goal of this work was achieved with the development of a WO_3 -based POC device that represents a reliable low-cost candidate for CF diagnosis (13 cents, not including costs related with the electricity of the equipment used) especially in resource-limited environments. Furthermore, some of the results here presented were published in a poster format at two conferences: the 32nd Edition of the Eurosensors Conference in Graz, Austria (9-12th September 2018); and the 6th Dresden Nanoscale Symposium in Dresden, Germany (31st August 2018). Both posters are presented in section G of Appendices.

References

- [1] A. St John and C. P. Price, "Existing and Emerging Technologies for Point-of-Care Testing," *Clin. Biochem. Rev.*, vol. 35, no. 3, pp. 155–167, 2014.
- [2] Z. Sonner, E. Wilder, T. Gaillard, G. Kasting, and J. Heikenfeld, "Integrated sudomotor axon reflex sweat stimulation for continuous sweat analyte analysis with individuals at rest," *Lab Chip*, vol. 17, no. 15, pp. 2550–2560, 2017.
- [3] F. Ratjen, S. C. Bell, S. M. Rowe, C. H. Goss, A. L. Quittner, and A. Bush, "Cystic fibrosis," *Nat. Rev. Dis. Prim.*, vol. 1, no. May, pp. 1–19, 2015.
- [4] N. Cirilli *et al.*, "Real life practice of sweat testing in Europe," *J. Cyst. Fibros.*, 2017.
- [5] L. Santos *et al.*, "Structure and morphologic influence of WO₃ nanoparticles on the electrochromic performance of dual-phase a-WO₃/WO₃ inkjet printed films," *Adv. Electron. Mater.*, vol. 1, no. 1–2, pp. 1–10, 2015.
- [6] L. Santos *et al.*, "WO₃ Nanoparticle-Based Conformable pH Sensor," *ACS Appl. Mater. Interfaces*, vol. 6, no. 15, pp. 12226–12234, 2014.
- [7] C. V Ramana, S. Utsunomiya, R. C. Ewing, C. M. Julien, and U. Becker, "Structural Stability and Phase Transitions in WO₃ Thin Films," *J. Phys. Chem. B*, vol. 110, no. 21, pp. 10430–10435, 2006.
- [8] "O que é a Fibrose Quística?," *ANFQ: Associação Nacional de Fibrose Quística*, 2017. [Online]. Available: <http://www.anfq.pt/o-que-e-a-fibrose-quistica/>. [Accessed: 14-Aug-2018].
- [9] "CF Genetics: The Basics," *Cystic Fibrosis Foundation [US]*, 2017. [Online]. Available: <https://www.cff.org/What-is-CF/Genetics/CF-Genetics-The-Basics/>. [Accessed: 14-Aug-2018].
- [10] "Diagnosed with Cystic Fibrosis," *Cystic Fibrosis Foundation [US]*, 2015. [Online]. Available: <https://www.cff.org/What-is-CF/Diagnosed-With-Cystic-Fibrosis/>. [Accessed: 14-Aug-2018].
- [11] N. Derichs, "Targeting a genetic defect: cystic fibrosis transmembrane conductance regulator modulators in cystic fibrosis," *Eur. Respir. Rev.*, vol. 22, no. 127, pp. 58–65, 2013.
- [12] V. De Matteis, A. Cannavale, L. Blasi, A. Quarta, and G. Gigli, "Chromogenic device for cystic fibrosis precocious diagnosis: A 'point of care' tool for sweat test," *Sensors Actuators B Chem.*, vol. 225, pp. 474–480, 2016.
- [13] C. Z. Esteves *et al.*, "Skin Biomarkers for Cystic Fibrosis : A Potential Non-Invasive Approach for Patient Screening," *Front. Pediatr.*, vol. 5, no. 290, pp. 1–8, 2018.
- [14] "O que é a Fibrose Quística: Como se diagnostica?," *ANFQ: Associação Nacional de Fibrose Quística*, 2017. [Online]. Available: <http://www.anfq.pt/o-que-e-a-fibrose-quistica/como-se-diagnostica/>. [Accessed: 14-Aug-2018].
- [15] A. Mishra, R. Greaves, and J. Massie, "The Relevance of Sweat Testing for the Diagnosis of Cystic Fibrosis in the Genomic Era," *Clin. Biochem. Rev.*, vol. 26, no. 4, pp. 135–153, 2005.
- [16] L. E. Gibson and R. E. Cooke, "A test for concentration of electrolytes in sweat in Cystic Fibrosis of the pancreas utilizing pilocarpine by iontophoresis," *Pediatrics*, vol. 23, no. 3, pp. 545–549, 1959.
- [17] A. Mena-Bravo and M. D. L. De Castro, "Sweat: A sample with limited present applications and promising future in metabolomics," *J. Pharm. Biomed. Anal.*, vol. 90, pp. 139–147, 2014.
- [18] F. J. Accurso *et al.*, "Sweat chloride as a biomarker of CFTR activity: Proof of concept and ivacaftor clinical trial data," *J. Cyst. Fibros.*, vol. 13, no. 2, pp. 139–147, 2014.
- [19] K. De Boeck, F. Vermeulen, and L. Dupont, "The diagnosis of cystic fibrosis," *Presse Med.*, vol. 46, no. 6P2, pp. e97–e108, 2017.
- [20] A. N. Macedo *et al.*, "The Sweat Metabolome of Screen-Positive Cystic Fibrosis Infants: Revealing Mechanisms beyond Impaired Chloride Transport," *ACS Cent. Sci.*, vol. 3, no. 8, pp. 904–913, 2017.
- [21] P. M. Farrell *et al.*, "Diagnosis of Cystic Fibrosis: Consensus Guidelines from the Cystic Fibrosis Foundation," *J. Pediatr.*, vol. 181S, pp. S4–15, 2017.
- [22] J. Gonzalo-Ruiz *et al.*, "Early determination of cystic fibrosis by electrochemical chloride quantification in sweat," *Biosens. Bioelectron.*, vol. 24, no. 6, pp. 1788–1791, 2009.
- [23] B. Schazmann *et al.*, "A wearable electrochemical sensor for the real-time measurement of sweat sodium concentration," *Anal. Methods*, vol. 2, no. 4, pp. 342–348, 2010.
- [24] J. Wang, X. Wu, C. Chon, T. Gonska, and D. Li, "A novel device for quantitative measurement of chloride concentration by fluorescence indicator," *Meas. Sci. Technol.*, vol. 23, no. 2, pp. 1–6, 2012.
- [25] A. J. Bandodkar *et al.*, "Epidermal tattoo potentiometric sodium sensors with wireless signal transduction for continuous non-invasive sweat monitoring," *Biosens. Bioelectron.*, vol. 54, no. 15,

- pp. 603–609, 2014.
- [26] M. J. Rock, L. Makhholm, and J. Eickhoff, “A new method of sweat testing: the CF Quantum® sweat test,” *J. Cyst. Fibros.*, vol. 13, no. 5, pp. 520–527, 2014.
- [27] X. Mu *et al.*, “A paper-based skin patch for the diagnostic screening of cystic fibrosis,” *Chem. Commun.*, vol. 29, no. 51, pp. 6365–6368, 2015.
- [28] W. Gao *et al.*, “Fully integrated wearable sensor arrays for multiplexed in situ perspiration analysis,” *Nature*, vol. 529, no. 7587, pp. 509–514, 2016.
- [29] S. Emaminejad *et al.*, “Autonomous sweat extraction and analysis applied to cystic fibrosis and glucose monitoring using a fully integrated wearable platform,” *Proc. Natl. Acad. Sci.*, vol. 114, no. 18, pp. 1–6, 2017.
- [30] S. Anastasova *et al.*, “A wearable multisensing patch for continuous sweat monitoring,” *Biosens. Bioelectron.*, vol. 93, pp. 139–145, 2017.
- [31] G. Matzeu *et al.*, “An integrated sensing and wireless communications platform for sensing sodium in sweat,” *Anal. Methods*, vol. 8, no. 1, pp. 64–71, 2016.
- [32] A. Koh *et al.*, “A soft, wearable microfluidic device for the capture, storage, and colorimetric sensing of sweat,” *Sci. Transl. Med.*, vol. 8, no. 366, pp. 1–13, 2016.
- [33] J. Choi, D. Kang, S. Han, S. B. Kim, and J. A. Rogers, “Thin, Soft, Skin-Mounted Microfluidic Networks with Capillary Bursting Valves for Chrono-Sampling of Sweat,” *Adv. Healthc. Mater.*, vol. 6, no. 5, pp. 1–10, 2017.
- [34] S. B. Kim *et al.*, “Super-Absorbent Polymer Valves and Colorimetric Chemistries for Time-Sequenced Discrete Sampling and Chloride Analysis of Sweat via Skin-Mounted Soft Microfluidics,” *Small*, vol. 14, no. 12, pp. 1–11, 2018.
- [35] J. Choi, R. Ghaffari, L. B. Baker, and J. A. Rogers, “Skin-interfaced systems for sweat collection and analytics,” *Sci. Adv.*, vol. 4, no. 2, pp. 1–9, 2018.
- [36] P. Bamfield, *Chromic Phenomena: The Technological Applications of Colour Chemistry*. Royal Society of Chemistry, 2001.
- [37] R. J. Mortimer, “Electrochromic materials,” *Annu. Rev. Mater. Res.*, vol. 41, pp. 241–268, 2011.
- [38] C.-G. Granqvist, “Electrochromic Metal Oxides: An Introduction to Materials and Devices,” in *Electrochromic Materials and Devices*, R. J. Mortimer, D. R. Rosseinsky, and P. M. Monk, Eds. Wiley-VCH, 2015, pp. 3–40.
- [39] C. G. Granqvist, “Electrochromic tungsten oxide films: Review of progress 1993-1998,” *Sol. Energy Mater. Sol. Cells*, vol. 60, no. 3, pp. 201–262, 2000.
- [40] P. M. S. Monk, R. J. Mortimer, and D. R. Rosseinsky, *Electrochromism: Fundamentals and Applications*, 1st ed. Weinheim: VCH, 1995.
- [41] P. R. Somani and S. Radhakrishnan, “Electrochromic materials and devices: present and future,” *Mater. Chem. Phys.*, vol. 77, no. 1, pp. 117–133, 2002.
- [42] K. Bange, “Colouration of tungsten oxide fillms: A model for optically active coatings,” *Sol. Energy Mater. Sol. Cells*, vol. 58, pp. 1–131, 1999.
- [43] P. M. S. Monk, R. J. Mortimer, and D. R. Rosseinsky, *Electrochromism and electrochromic devices*. Cambridge: Cambridge University Press, 2007.
- [44] C. G. Granqvist, *Handbook of Inorganic Electrochromic Materials*, 1st ed. Amsterdam: Elsevier B.V, 1995.
- [45] Q. Tang *et al.*, “1-Ethyl-3-methylimidazolium tetrafluoroborate-doped high ionic conductivity gel electrolytes with reduced anodic reaction potentials for electrochromic devices,” *Mater. Des.*, vol. 118, pp. 279–285, 2017.
- [46] K. K. Kumar, M. Ravi, Y. Pavani, S. Bhavani, A. K. Sharma, and V. V. R. N. Rao, “Electrical conduction mechanism in NaCl complexed PEO/PVP polymer blend electrolytes,” *J. Non. Cryst. Solids*, vol. 358, no. 23, pp. 3205–3211, 2012.
- [47] S. Chapi, S. Raghu, and H. Devendrappa, “Enhanced electrochemical, structural, optical, thermal stability and ionic conductivity of (PEO/PVP) polymer blend electrolyte for electrochemical applications,” *Ionics (Kiel)*, vol. 22, no. 6, pp. 803–814, 2016.
- [48] S. Stice, M. A. Thrall, and D. W. Hamar, “Alcohols and Glycols,” in *Veterinary Toxicology: Basic and Clinical Principles*, 3rd ed., R. C. Gupta, Ed. Elsevier Inc., 2018, pp. 647–657.
- [49] J. Burgess, *Metal Ions in Solution*, 1st ed. New York: Ellis Horwood Ltd, 1978.
- [50] A. Marques *et al.*, “A planar electrochromic device using WO₃ nanoparticles and a modified paper-

- based electrolyte". Poster session presented at: *EUROSENSORS 2018*; 32nd Edition; 2018 Sep 9-12; Graz, Austria.
- [51] A. C. Marques *et al.*, "Office paper platform for bioelectrochromic detection of electrochemically active bacteria using tungsten trioxide nanopores," *Sci. Rep.*, vol. 5, no. 9910, pp. 1–7, 2015.
- [52] S. Wang, W. Fan, Z. Liu, A. Yu, and X. Jiang, "Advances on tungsten oxide based photochromic materials: strategies to improve their photochromic properties," *J. Mater. Chem. C*, vol. 6, pp. 191–212, 2018.
- [53] I. M. Szilágyi *et al.*, "WO₃ photocatalysts: Influence of structure and composition," *J. Catal.*, vol. 294, pp. 119–127, 2012.
- [54] Y. S. Zou *et al.*, "Structural and optical properties of WO₃ films deposited by pulsed laser deposition," *J. Alloys Compd.*, vol. 583, pp. 465–470, 2014.
- [55] W. Sun *et al.*, "High Surface Area Tunnels in Hexagonal WO₃," *Nano Lett.*, vol. 15, no. 7, pp. 4834–4838, 2015.
- [56] S. Salmaoui, F. Sediri, and N. Gharbi, "Characterization of h-WO₃ nanorods synthesized by hydrothermal process," *Polyhedron*, vol. 29, no. 7, pp. 1771–1775, 2010.
- [57] S. Rajagopal, D. Nataraj, D. Mangalaraj, Y. Djaoued, J. Robichaud, and O. Y. Khyzhun, "Controlled Growth of WO₃ Nanostructures with Three Different Morphologies and Their Structural, Optical, and Photodecomposition Studies," *Nanoscale Res. Lett.*, vol. 4, no. 11, pp. 1335–1342, 2009.
- [58] H. Hayashi and Y. Hakuta, "Hydrothermal Synthesis of Metal Oxide Nanoparticles in Supercritical Water," *Materials (Basel)*, vol. 3, pp. 3794–3817, 2010.
- [59] B. I. Kharisov, O. V. Kharissova, and U. O. Méndez, "Microwave Hydrothermal and Solvothermal Processing of Materials and Compounds," in *The Development and Application of Microwave Heating*, W. Cao, Ed. IntechOpen, 2012, pp. 107–140.
- [60] C. O. Kappe, A. Stadler, and D. Dallinger, *Microwaves in Organic and Medicinal Chemistry*, 2nd ed. Wiley-VCH, 2012.
- [61] M. Guiotoku, C. M. B. F. Maia, C. R. Rambo, and D. Hotza, "Synthesis of Carbon-based Materials by Microwave Hydrothermal Processing," in *Microwave Heating*, U. Chandra, Ed. IntechOpen, 2011, pp. 291–308.
- [62] D. Nagy, T. Firkala, E. Drotár, Á. Szegedi, K. László, and I. M. Szilágyi, "Photocatalytic WO₃/TiO₂ nanowires: WO₃ polymorphs influencing the atomic layer deposition of TiO₂," *RSC Adv.*, vol. 6, no. 98, pp. 95369–95377, 2016.
- [63] H. Hori, M. Takase, M. Takashima, F. Amano, T. Shibayama, and B. Ohtani, "Mechanism of formation, structural characteristics and photocatalytic activities of hierarchical-structured bismuth-tungstate particles," *Catal. Today*, vol. 300, pp. 99–111, 2017.
- [64] L. S. L. Santos, "Engineering of Metal Oxide Nanoparticles for Application in Electrochemical Devices," Faculdade de Ciências e Tecnologia, Universidade Nova de Lisboa, 2015.
- [65] S. Yuan *et al.*, "A Photometric High-Throughput Method for Identification of Electrochemically Active Bacteria Using a WO₃ Nanocluster Probe," *Sci. Rep.*, vol. 3, no. 1, pp. 1–7, 2013.
- [66] L. T. L. Anh *et al.*, "Tailoring the structure and morphology of WO₃ nanostructures by Hydrothermal Method," *Vietnam J. Sci. Technol.*, vol. 56, no. 1A, pp. 127–134, 2018.
- [67] Y. Li, Z. Tang, J. Zhang, and Z. Zhang, "Exposed facet and crystal phase tuning of hierarchical tungsten oxide nanostructures and their enhanced visible-light-driven photocatalytic performance," *CrystEngComm*, no. 47, pp. 1–9, 2015.
- [68] Y. Li, Z. Tang, J. Zhang, and Z. Zhang, "Enhanced photocatalytic performance of tungsten oxide through tuning exposed facets and introducing oxygen vacancies," *J. Alloys Compd.*, vol. 708, pp. 358–366, 2017.
- [69] P. J. Wojcik, L. Pereira, R. Martins, and E. Fortunato, "Metal Oxide Nanoparticle Engineering for Printed Electrochemical Applications," in *Handbook of Nanoelectrochemistry*, M. Aliofkhaezrai and A. S. H. Makhlof, Eds. Springer International Publisher, 2015, pp. 1–29.
- [70] J. C. Slater, *Quantum Theory of Molecules and Solids Volume 2: Symmetry & Energy Bands in Crystals*, 1st ed. New York: McGraw Hill, 1965.
- [71] J. C. Slater, "Atomic Radii in Crystals," *J. Chem. Phys.*, vol. 41, no. 10, pp. 3199–3204, 1964.
- [72] R. B. Goldner *et al.*, "Electrochromic behavior in ITO and related oxides," *Appl. Opt.*, vol. 24, no. 15, pp. 2283–2284, 1985.
- [73] Z. Jiao, X. W. Sun, J. Wang, L. Ke, and H. V. Demir, "Hydrothermally grown nanostructured WO₃

- films and their electrochromic characteristics," *J. Phys. D. Appl. Phys.*, vol. 43, no. 28, 2010.
- [74] C. A. Riedi, A. F. Zavadniak, D. C. Silva, A. Franco, and N. A. R. Filho, "Comparison of conductivity with sodium determination in the same sweat sample," *J. Pediatr. (Rio. J.)*, vol. 76, no. 6, pp. 443–446, 2000.
- [75] H. Shwaehman, A. Mahmoodian, and R. K. Neff, "The sweat test: Sodium and chloride values," *J. Pediatr.*, vol. 98, no. 4, pp. 576–578, 1981.
- [76] M. Constantinescu and B. C. Hilman, "The Sweat Test for Quantitation of Electrolytes: A Challenge in Precision," *Lab. Med.*, vol. 27, no. 7, pp. 472–477, 1996.
- [77] V. Vasiliou, K. Vasiliou, and D. W. Nebert, "Human ATP-binding cassette (ABC) transporter family," *Hum. Genomics*, vol. 3, no. 3, pp. 281–290, 2009.
- [78] S. S. Kalanur, Y. J. Hwang, S. Y. Chae, and O. S. Joo, "Facile growth of aligned WO₃ nanorods on FTO substrate for enhanced photoanodic water oxidation activity," *J. Mater. Chem. A*, vol. 1, no. 10, pp. 3479–3488, 2013.
- [79] E. M. M. Abdelrazek, A. M. Abdelghany, S. I. Badr, and M. A. Morsi, "Structural, optical, morphological and thermal properties of PEO/PVP blend containing different concentrations of biosynthesized Au nanoparticles," *J. Mater. Res. Technol.*, pp. 1–13, 2017.

Appendices

A. CFTR protein

As illustrated in Figure 28, CFTR protein has five domains: two nucleotide-binding domains (NBDs), capable of binding and hydrolysing ATP; two membrane-spanning domains (MSDs) each composed of six subunits, which form the channel pore; and one regulatory domain (R), a group of amino acids. The channel opens when its R domain is phosphorylated by protein kinase A and when ATP is bound at the NBDs. [3], [11], [77]

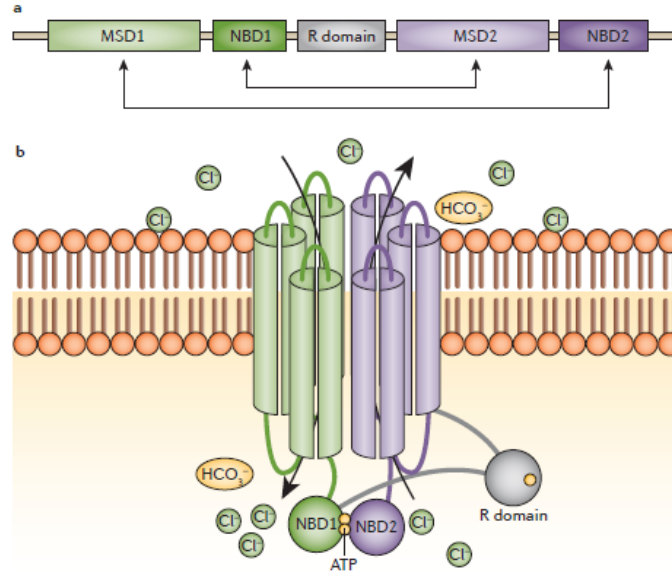


Figure 28: CFTR protein structure: a) Linear structure; b) 3D structure in the cell membrane. [3]

B. WO_3 crystallographic structures: monoclinic, orthorhombic and hexagonal

As already mentioned, WO_6 units undergo some changes in the position of the central W atoms, promoting several crystalline modifications to WO_3 . Three of them are described right after.

The structure of stable monoclinic WO_3 is a ReO_3 -type structure with corner-sharing WO_6 octahedra connected in the a-, b- and c-directions, as already described and as depicted in Figure 29. This leads to the formation of a stacked layer structure. [52], [55]

In the orthorhombic $\text{WO}_3 \cdot 0.33\text{H}_2\text{O}$ structure, an infinite plane of WO_6 octahedra share their corners and form six-membered rings along the (001) plane, as shown in Figure 29. Each (001) plane contains two types of WO_6 octahedra. Type I consists of a WO_6 octahedron connecting six different octahedra by corner-sharing. The four oxygen atoms along the plane (001) are shared by four neighbouring octahedra in the same layer, while the other two, that are perpendicular to the (001) plane, are shared with the adjacent layers above and below. This ensures the connection between the layers and thus the stability of this structure. Type II octahedra, $\text{WO}_5(\text{H}_2\text{O})$, consist of four oxygen atoms in the (001) plane, and the two that are off the (001) plane are substituted by a short terminal $\text{W}=\text{O}$ bond and a longer $\text{W}-\text{H}_2\text{O}$ bond. Contrary to Type I, the two oxygen atoms off the (001) plane do not bond to other W atoms of adjacent layers above and below. As a result, an infinite layer is formed by corner-sharing the two octahedra types in the (001) plane. [78] Such an arrangement results in strong interactions within layers, and relatively weaker interactions between adjacent layers, resulting in a less compact structure that benefits the ion intercalation/deintercalation during the electrochromic process. [5]

The hexagonal WO_3 structure is built up of slightly distorted WO_6 octahedra arranged in six-membered rings by sharing corner oxygens along the (001) plane. This leads to the formation of large hexagonal shaped tunnels throughout the entire unit cell, which also allows a better ion intercalation/deintercalation during the electrochromic process. [55], [78]

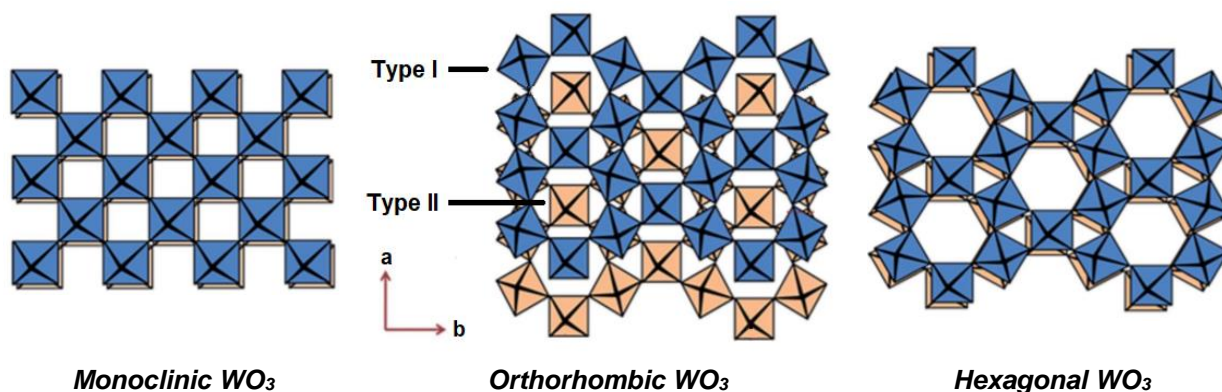


Figure 29: Crystallographic structures of WO_3 : monoclinic, orthorhombic, and hexagonal. Adapted from [78].

C. Materials

Table 5: List of all used reagents and respective chemical formula, purity, CAS, and company.

Reagent	Chemical formula	Purity	CAS	Company
Ethanol	C ₂ H ₅ OH	96%	64-17-5	Carlo Erba Reagents (Dasit Group)
Ethylene glycol butyl ether (EGBE)	C ₆ H ₁₄ O ₂	≥ 99%	111-76-2	Sigma-Aldrich
Hydrochloric acid	HCl	37%	7647-01-0	Fisher Chemical
Lithium perchlorate	LiClO ₄	≥ 98%	7791-03-9	Sigma-Aldrich
Magnesium sulphate anhydrous	MgO ₄ S	≥ 98%	7487-88-9	Fluka
PE-AG-530 Flexible Silver (Ag) Conductive Ink*	-	-	-	Conductive Compounds
ITO coated PET # (30.5 cm x 30.5 cm x 127 μm)	In ₂ O ₃ /SnO ₂	-	-	Sigma-Aldrich
Polyethylene oxide (PEO) M _v ~100 000	(-CH ₂ CH ₂ O-) _n	-	25322-68-3	Aldrich Chemicals
Polyvinylpyrrolidone (PVP) M _w ~1 300 000	(C ₆ H ₉ NO) _n	-	9003-39-8	Aldrich Chemicals
Potassium chloride (crystals)	KCl	-	7447-40-7	José M. Vaz Pereira, S.A.
Propylene carbonate (PC)	C ₄ H ₆ O ₃	99.5%	108-32-7	Acros Organics
Propylene glycol (PG)	C ₃ H ₈ O ₂	-	57-55-6	LabChem
Sodium chloride	NaCl	99.5%	7647-14-5	Panreac
Sodium sulphate anhydrous	Na ₂ SO ₄	99%	7757-82-6	Panreac
Sodium tungstate dihydrate	Na ₂ WO ₄ ·2H ₂ O	≥ 99%	10213-10-2	AnalaR NORMAPUR® (VWR Chemicals)

*Surface resistivity: < 0.025 Ω/sq/mil

#Surface resistivity: 60 Ω/sq

D. NaCl-based electrolytes' preparation

By adjusting the experimental procedure described elsewhere, a viscous liquid non-aqueous NaCl-based electrolyte was produced to test the devices. [46] PG was used as solvent, and the quantities of each reagent were adapted. The best procedure found is described below.

1. Add 6.5 g of PEO to 100 mL of PG and stir for 12 h at 600 rpm and 35 °C;
2. Add 2.17 g of PVP to the mixture, maintaining the same conditions for 12 h;
3. Pour the mixture into 7 flasks and add NaCl in order to make seven different concentrations with a final volume of 10 mL: 0, 30, 45, 60, 75, 90, and 120 mM;
4. Stir, maintaining the same conditions, over one night. The electrolyte obtained for a 60 mM concentration of NaCl is presented in Figure 30 a).

To study the influence of Mg²⁺ and K⁺ in the WO₃ NPs colouration, two more electrolytes were produced: one with KCl (10 mM) and other with MgO₄S (2 mM). The concentrations used were as described and tested elsewhere. [12] For each electrolyte, the PEO+PVP+PG mixture already prepared was poured into a flask with a final volume of 5 mL, followed by the addition of the respective reagent and a stirring step at 600 rpm and 35 °C, over one night.

A fourth electrolyte was produced and it consisted in joining all reagents to make a mixture with 4 different NaCl concentrations: 0, 30, 60, and 120 mM. For each electrolyte, the PEO+PVP+PG mixture already prepared was poured into a flask with a final volume of 5 mL, followed by the addition of KCl (10 mM), MgO₄S (2 mM), and the respective amount of NaCl, with a final stirring step at 600 rpm and 35 °C, over one night.

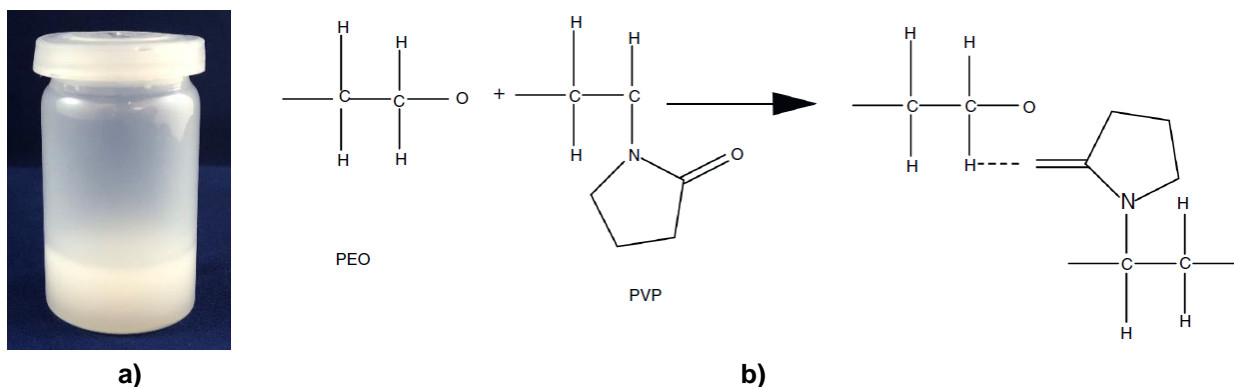


Figure 30: a) Final aspect of the electrolyte produced with PG, PEO, PVP, and a 60 mM concentration of NaCl. b) Formation of the polymer blend between PEO and PVP. The blend occurs through a hydrogen bond between the carbonyl group of PVP and the methylene group of PEO. [79]

E. XRD analysis

In order to facilitate the perception of the optimization process using MAHS, all XRD analysis data presented was arranged in a different way.

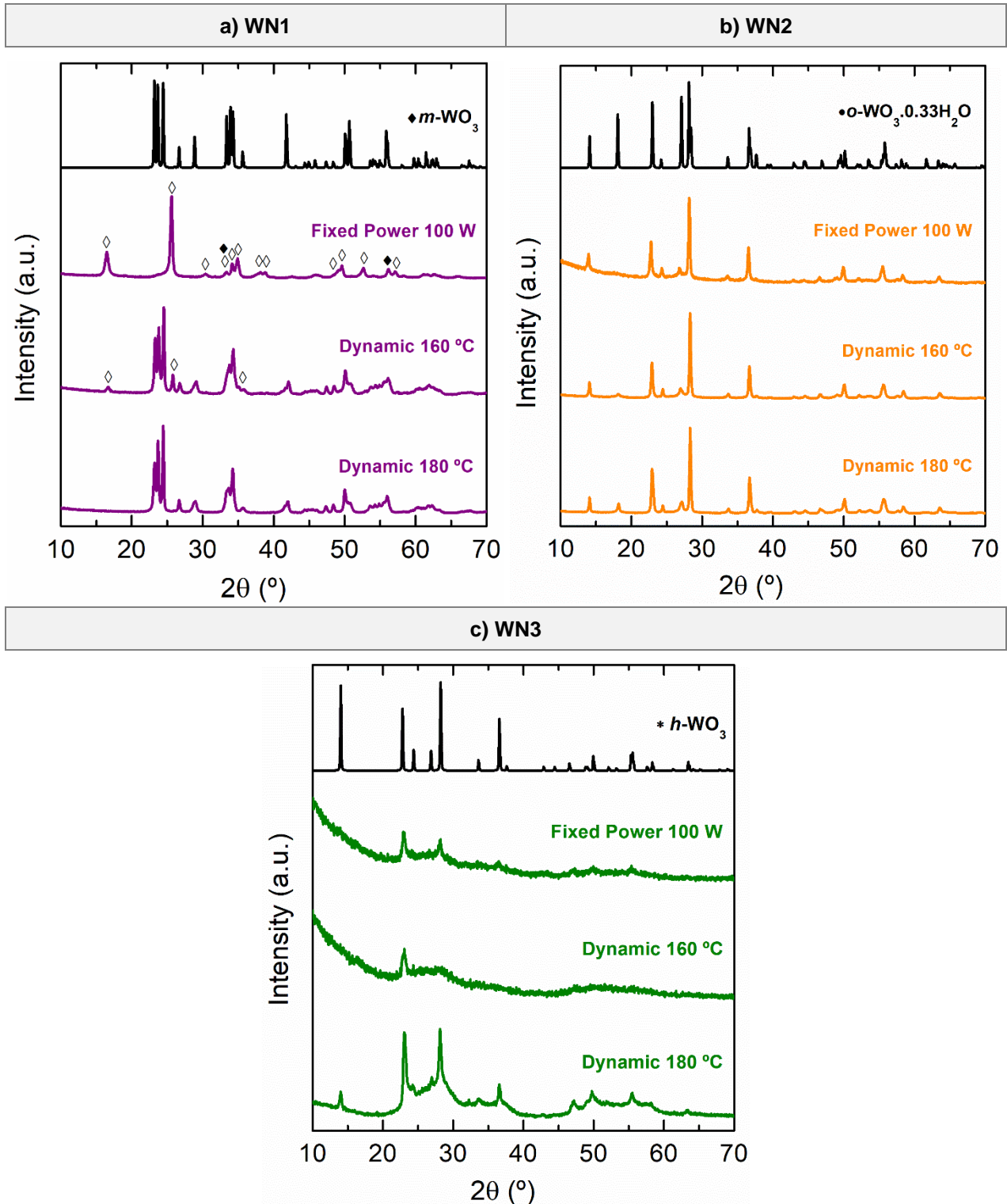


Figure 31: Resume of the synthesis' optimization process using MAHS for sample a) WN1, b) WN2, and c) WN3. The diffractograms represented in black are the crystallographic files deposited in the ICDD data base with the references #98-007-1506, #98-003-7822, and #98-001-3851, for monoclinic, hydrated orthorhombic, and hexagonal crystallographic structures of WO_3 , respectively. Peaks marked with \blacklozenge and \blacklozenge are characteristic of $\text{H}_2\text{WO}_4 \cdot n\text{H}_2\text{O}$ and $m\text{-WO}_3$ crystallographic structures, respectively.

F. Cyclic voltammetry

Additional cyclic voltammetry analysis performed on the devices before encapsulation. The curves were obtained using the electrolyte composed by PEO, PVP, PG, and NaCl at 60 mM, from 3 to -2.5 V at different scan rates (25, 50, 75, 100, and 125 mV/s) during 4 cycles each.

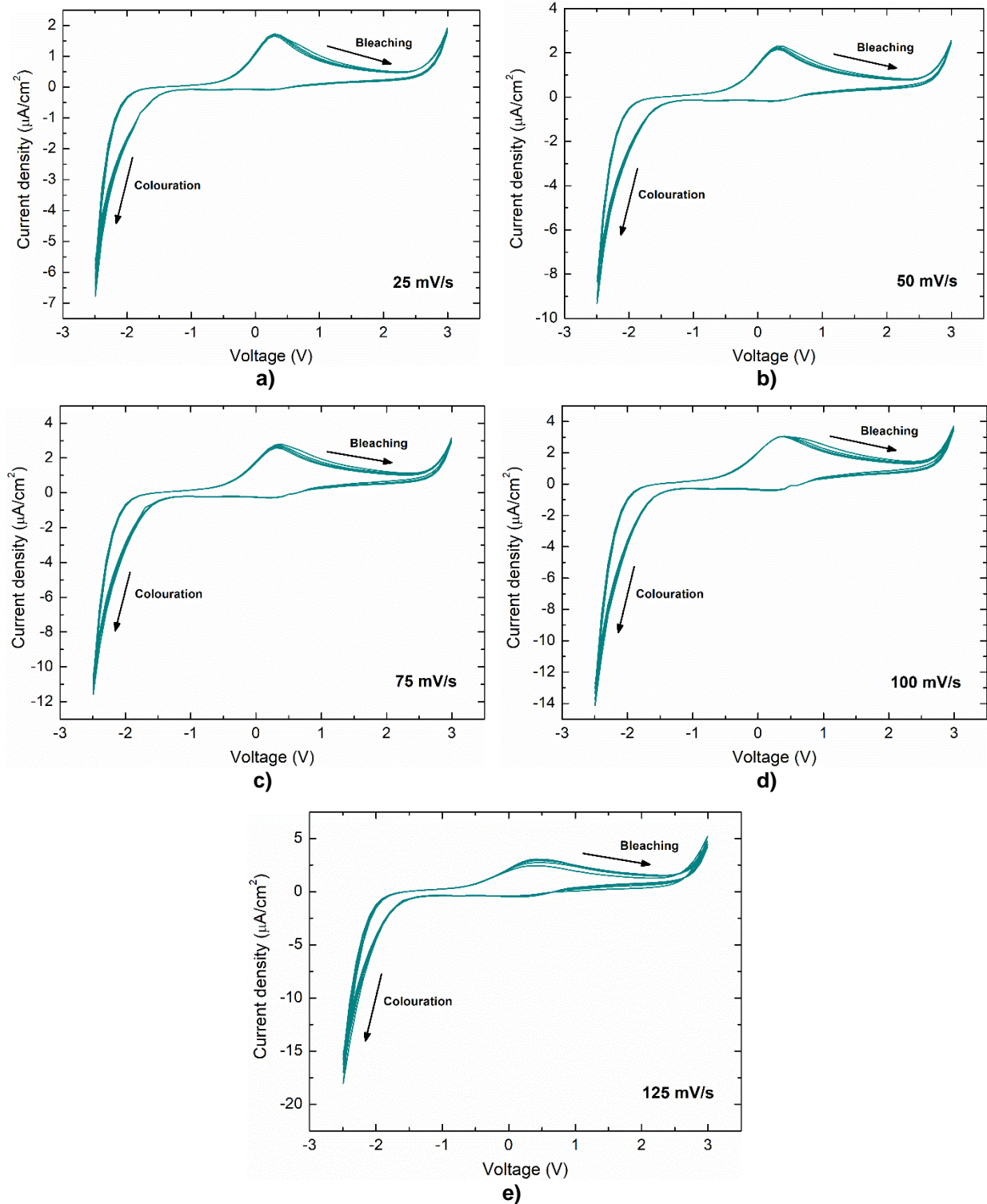


Figure 32: Cyclic voltammetry curves obtained for the devices before encapsulation. Measurements were performed using the electrolyte composed by PEO, PVP, PG, and NaCl at 60 mM, from 3 to -2.5 V during 4 cycles, at a scan rate of a) 25 mV/s, b) 50 mV/s, c) 75 mV/s, d) 100 mV/s, and e) 125 mV/s.

G. Published posters

32nd Edition of the Eurosensors Conference, 9-12th September 2018, Graz, Austria

Eurosensors 2018

A PLANAR ELECTROCHROMIC DEVICE USING WO₃ NANOPARTICLES AND A MODIFIED PAPER-BASED ELECTROLYTE

Ana Marques^{1,7}, Lídia Santos^{1,2}, Sónia Pereira¹, Alexandra Fernandes¹, Umberto Emanuele³, Stefano Sinopoli³, Rui Igreja¹, Goreti Sales⁴, Rodrigo Martins¹ and Elvira Fortunato^{1,4*}

¹CENIMAT/13N, Departamento de Ciência de Materiais, Faculdade de Ciências e Tecnologia, Universidade NOVA de Lisboa and CEMOP/UNINOVA, Campus da Caparica, 2829-516 Caparica – Portugal
²Hovione, Campus do Lumiar, Edifício S, Estrada do Paço do Lumiar, 1649-038 Lisboa, Portugal
³Bioage, Lamezia, Terme 88046, Italy
⁴BioMark/CEB, ISEP, R. Dr. António Bernardino de Almeida, 431, 4200-072 Porto, Portugal
*accm@campus.fct.unl.pt; emf@fct.unl.pt

Abstract

Electrochromic (EC) devices are increasing its interest in the last decades due to the wide range of applications, from smart windows to biosensors or from smart labels to super-capacitors. So, the development of **simple and cost-effective production technologies** based on solution process and **mask less** approach is of great interest. In this work, a **new planar and flexible** electrochromic device based on tungsten oxide (WO₃) nanoparticles with a **paper-based modified electrolyte** was successfully produced, using a **CO₂ laser technology** for electrodes patterning and hydrothermal synthesis for the nanoparticles production. The devices were fabricated with a paper pad inserted in the sensor area for hydration on time of usage, thus replacing the electrolyte material of a typical electrochromic structure with a multi-layer stack, **eliminating leakage problems**, **easy integration** with other devices and **enhancing the shelf life** of the devices to several months. The produced device presents a **low power consumption** of only 2.86 μA.cm⁻², with a **deep blue colour** and an initial charge modulation of 11.5.

Device fabrication

Device characterization

Low power consumption: 2.8 μA.cm⁻²
High color modulation

Application: cystic fibrosis biosensor

Genetic disorder
Usually diagnosed in newborns

Sweat test: gold standard

Chloride concentration	Result
< 40 mM	Normal
40 – 60 mM	Borderline or indeterminate
> 60 mM	Abnormal

Cystic fibrosis diagnostic kit:

- EC planar device
- Small 3V button cell apparatus
- Smartphone

Digital colorimetric analysis through RGB control

WO₃ + xNa⁺ + xe⁻ ↔ Na_xWO₃

Final remarks

- A new planar architecture was developed using laser technology for electrodes patterning. The method allows a **freedom of design, mask less**, simple and cost-effective process for devices fabrication.
- The EC devices presented a **high optical modulation**, with a fast response time and a stable behavior. This device structure, even if not fully optimized, can be **easily adapted** for several commercial applications just by choosing the best combination of materials.

Acknowledgments AM acknowledges funding to National Foundation for Science and Technology, I.P., through the PhD Grant SFRH/BG/15173/2016.

www.cenimat.fct.unl.pt

Development and optimization of point-of-care nanobiosensing platforms

A. Marques^{1*}, A. Fernandes¹, N. Ferreira¹, R. Martins¹, B. Costa-Silva², G. Sales³, E. Fortunato^{1*}

¹ CENIMAT/13N, Departamento de Ciência de Materiais, Faculdade de Ciências e Tecnologia, Universidade NOVA de Lisboa and CEMOP/UNINOVA, Campus da Caparica, 2829-516 Caparica – Portugal

² Champalimaud Foundation, Centre for the Unknown, 1400-038 Lisbon, Portugal

³ BioMark/CINTESIS, 4200-072 Porto, Portugal

*accm@campus.fct.unl.pt; emf@fct.unl.pt

Motivation use of inexpensive materials and cost-effective manufacturing processes towards low-cost disposable platforms for healthcare and environmental applications.

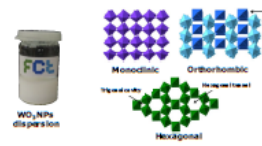
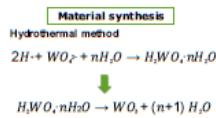


Research activities

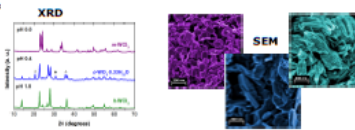
- ◊ Colorimetric paper-based biosensors
- ◊ Electrochromic devices
- ◊ MIP-SERS platform for cancer screening

Electrochromism

Electrochromic (EC) materials are increasing its interest in the last decades due to the **wide range of applications**, from smart windows to **biosensors** or from **smart labels** to super-capacitors. Tungsten oxide (WO₃) is one of the most studied EC inorganic materials due to its high coloration efficiency and good cycle stability.

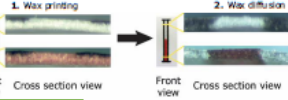


Tailoring of WO₃ crystallography and morphology



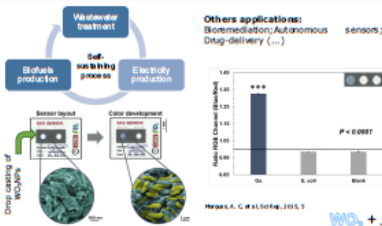
Lab-on-Paper

Lab-on-paper is a novel technology to produce **inexpensive, easy to fabricate and easy to use** paper-based devices for **point-of-care** diagnostic, by an eco-friendly **wax-printing technology**.



Bacteria screening

Electrochemically Active Bacteria possess the capability to transfer their electrons to outside of their cells.



Others applications: Biomedication/Autonomous sensors; Drug-delivery (...)

Applications

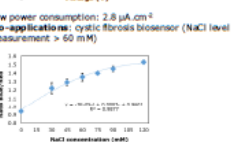
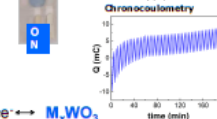
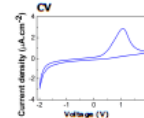
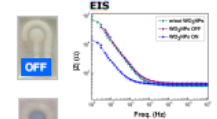
EC device

A **new planar electrochromic device** based on tungsten oxide nanoparticles is presented, with **laser technology** for electrodes patterning and with a paper pad inserted in the sensor area for **hydration on time of usage**.

Device fabrication

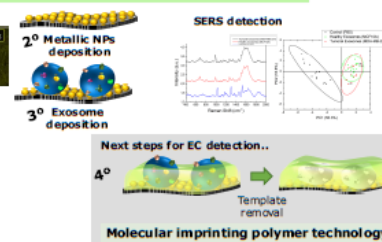
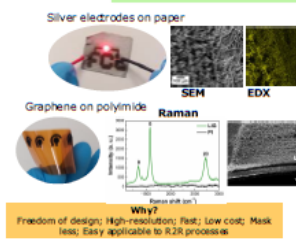
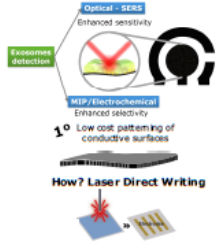


Device characterization and testing



MIP-SERS platform

Main goal: detection of tumorous exosomes for cancer diagnosis and follow-up



Final remarks

- The use of **paper** as substrate for diagnostic platforms is very attractive and has spurred a variety of technologies. Its use has great emphasis in **point-of-need** settings, particularly in resource-poor countries.
- **WO₃** is a very versatile material that can be used in low cost biosensors for environmental and healthcare applications.
- Laser technology allows a multitude of approaches from **electrodes patterning** by ablation to laser direct writing of electrodes by **laser processing and sintering** of nanoparticles.

Acknowledgments AM acknowledges funding to National Foundation for Science and Technology, I.P., through the PhD Grant SFRH/BD/115173/2016.

